

# INSTRUMENTATION FOR ABSORPTION SPECTROSCOPY MEASUREMENTS IN THE ULTRAVIOLET

by

Renata Bartula

A thesis submitted in partial fulfillment of the  
requirements for the degree of

Master of Science  
(Mechanical Engineering)

at the

UNIVERSITY OF WISCONSIN-MADISON

# **ABSTRACT**

## **Instrumentation for Absorption Spectroscopy Measurements in the Ultraviolet**

Renata Bartula

Under the supervision of Associate Professor Scott T. Sanders

at the University of Wisconsin-Madison

In order to measure ultraviolet spectra, an instrumentation method must be carefully selected. The first consideration is whether to use a hyperspectral source in combination with a single-element photodiode or a broadband source in combination with a grating spectrometer. Next, all sources of noise are considered in the experiment in order to improve the signal to noise ratio of the measurement. Finally, the source of ultraviolet light is considered as well as the spectrometer used for data analysis given that the hyperspectral source is not chosen.

Designing a broadband high speed high resolution instrument is the next step in ultraviolet experimentation. All data analysis options were considered in great detail including the grating spectrometer, the Fourier Transform Ultraviolet interferometer, and the Spatial Heterodyne Spectrometer. By carefully examining these instruments, it was apparent that a Spatial Heterodyne Spectrometer (SHS) was the best option for high speed high resolution instrumentation. The SHS instrument was then simulated, designed, and aligned. The SHS design difficulties are discussed, and recommendations for future work are presented.

## DEDICATION

To my brother Chris.

## **ACKNOWLEDGEMENTS**

I would like to thank my advisor, Dr. Scott Sanders, for the opportunity to work in the Engine Research Center and for all of the knowledge that he has passed on to me. Scott's patience and understanding made my experience at the University of Wisconsin extremely enjoyable.

I also want to thank everyone that I worked with in the labs including Drew Caswell, Keith Rein, Thilo Kraetschmer, Karissa Thoma, Adam Witikiewicz, Daryl Dagel, Xinliang An, and Ben Conrad. All of your help and cooperation made my work progress smoothly.

I want to thank everyone in the Engine Research Center for assisting me while I continued my education. I especially want to thank Deanna Duerst for all the help with paperwork, Ralph Braun for improving my machining skills, and Josh Leach for helping me with my computer issues.

Finally, I want to thank my family and friends for their continuous support. I want to thank my parents for supporting me throughout my college career and telling me to continue my education. I especially want to thank my understanding husband Justin Wirth for always being there for me and helping me through the hard times.

## TABLE OF CONTENTS

<b>Abstract.....</b>	<b>i</b>
<b>Dedication .....</b>	<b>ii</b>
<b>Acknowledgements .....</b>	<b>iii</b>
<b>Table of Contents .....</b>	<b>iv</b>
<b>Table of Figures.....</b>	<b>vi</b>
<b>Chapter 1. Introduction.....</b>	<b>1</b>
1.1 Hyperspectral source versus broadband source combined with a grating spectrometer .....	1
1.2 Sources of noise .....	2
1.3 Broadband ultraviolet light sources .....	3
1.4 Ultraviolet spectrometers .....	4
<b>Chapter 2. Designing a broadband high speed high resolution instrument.....</b>	<b>6</b>
2.1 Grating spectrometer considerations.....	6
2.1.1 Low throughput.....	6
2.1.2 Large instrument size for high resolution .....	7
2.2 FTUV interferometer considerations .....	7
2.2.1 High resolution spectra .....	8
2.2.2 Moving mirror issues .....	9
2.3 High speed SHS design.....	10
2.3.1 Light source and test engine selection .....	10
2.3.2 SHS simulation .....	12
2.3.3 Optics selection.....	13
2.3.4 Design difficulties .....	15
2.4 Other high-speed measurement options.....	16
2.4.1 Grating spectrometer for low resolution measurement.....	16
<b>Chapter 3. Conclusions and future work.....</b>	<b>17</b>
<b>References.....</b>	<b>18</b>
<b>Appendix I. Modeless wavelength-agile laser experiment: <i>Modeless operation of a wavelength-agile laser by high-speed cavity length changes</i> .....</b>	<b>19</b>
I.1 Abstract.....	19
I.2 Nomenclature.....	19
I.3 Introduction.....	20
I.4 Laser design .....	22
I.4.1 Computer animation .....	23
I.4.2 Laser construction .....	25
I.4.3 Modeless operation .....	26

I.5	Sample results .....	29
I.6	Discussion .....	31
I.7	Conclusions .....	33
I.8	Acknowledgements .....	33
I.9	References and links .....	33
<b>Appendix II. Multimode fiber noise experiment: Estimation of signal noise induced by multimode optical fibers .....</b>		<b>36</b>
II.1	Abstract .....	36
II.2	Nomenclature and variables .....	36
II.3	Introduction .....	38
II.4	Simulation development .....	42
II.5	Summary and outlook .....	51
II.6	Acknowledgements .....	52
II.7	References .....	52
II.8	Appendix I .....	53
<b>Appendix III. Supercontinuum generation experiment: Generation of ultraviolet broadband light in a single mode fiber .....</b>		<b>57</b>
III.1	Abstract .....	57
III.2	Introduction .....	57
III.3	Generation of broadband light .....	62
III.3.1	Basic principles .....	62
III.3.2	UV design guide .....	63
III.3.3	Optical arrangement .....	67
III.4	Results .....	68
III.5	Summary and outlook .....	73
III.6	Acknowledgements .....	75
III.7	References .....	76
<b>Appendix IV. Spatial Heterodyne Spectroscopy experiment: OH absorption spectroscopy in a flame using Spatial Heterodyne Spectroscopy .....</b>		<b>79</b>
IV.1	Abstract .....	79
IV.2	Introduction .....	79
IV.3	Motivation .....	80
IV.4	SHS data .....	84
IV.5	Summary and outlook .....	89
IV.6	Acknowledgements .....	90
IV.7	References .....	90
IV.8	Appendix A .....	92

## TABLE OF FIGURES

Figure 1.1 Sensor Electronic Technologies UVTOP-310 LED spectrum. Inset is a picture of the LED. ....	4
Figure 2.1 Schematic of the FTUV interferometer arrangement. The UV LED is collimated then sent through the engine ring test section where OH absorption will occur. The light is then sent through a multimode fiber by a collimation package. The fiber is split, half of it going to photodiode 1 and the other half is collimated and travels into the FTUV instrument indicated by the gray box. As the nano-positioner moves a spectrum is recorded by photodiode 2, which is preceded by a filter to reject chemiluminescence. ....	7
Figure 2.2 Simulated OH spectrum convoluted with the UV LED spectrum. The white line represents the transformed $B(\nu)$ , and the red line represents the original $B(\nu)$ . From the graph, it is apparent that high resolution spectra are achievable given the proper equipment. ....	9
Figure 2.3 GM metal engine schematic. The GM metal engine achieves optical access by two holes drilled directly into the engine head. The light, indicated by the red dotted line, is sent through the first smaller window into the combustion chamber then back out through the second larger window. ....	11
Figure 2.4 Triptane engine schematic. The Triptane engine uses an engine ring for optical access rather than drilling holes in the engine head. The head and the ring are separated by a copper retaining ring. The light, indicated by the red dotted line, is sent through the first window into the combustion chamber then back out through the second window in the engine ring. ....	12
Figure 2.5 Sample MATLAB simulation output. ....	13
Figure 2.6 High-speed SHS schematic. ....	14

## CHAPTER 1. INTRODUCTION

### 1.1 HYPERSPECTRAL SOURCE VERSUS BROADBAND SOURCE COMBINED WITH A GRATING SPECTROMETER

To begin ultraviolet (UV) experimentation, an instrumentation method must be chosen. One method involves the use of a hyperspectral source and a single detector. An example of such a method involves an external cavity modeless wavelength-agile laser. In the Engine Research Center, we developed a near-infrared version of this type of laser in order to scan from 1370 to 1464 nm as described by the paper in Appendix I. This laser was used to measure water absorption in an engine, but the design could also be applied to ultraviolet wavelengths provided that there is a commercial diode laser produced at the desired wavelength. One source for UV laser diodes, Nichia Corporation, provided a diode that could potentially be scanned from 370 to 374 nm.

The other instrumentation method involves a broadband light source in combination with a grating spectrometer. This method uses a light source with a broad spectrum that is analyzed by a grating spectrometer featuring a multi-pixel camera. Ultraviolet OH absorption was measured this way at the Engine Research Center with a resolution of  $\sim 250 \text{ cm}^{-1}$  [1]. This instrumentation method was chosen for the work described in this thesis based on a couple of reasons. A commercial laser diode was not available at the desired wavelength for hyperspectral sensing, and the hyperspectral laser is less stable than other instrumentation methods due to its mechanical mirror movement. Therefore, the broadband light source in combination with the grating spectrometer was chosen as the desired method for ultraviolet experimentation in this case.



## 1.2 SOURCES OF NOISE

Since the instrumentation method has been chosen, all possible sources of noise in the experiment will be identified. The first category of noise considered was inherent optical noise which includes polychromatic beating noise and shot noise. Polychromatic beating noise is the interference among the light waves; the magnitude of this noise is a function of spectral bandwidth and detection bandwidth [2], [3]. Shot noise occurs due to the quantization of optical energy into finite packets (photons); its relative amplitude equals the square root of the number of photons collected per measurement. The next category of noise is optical handling noise which includes beamsteering noise, vibration noise, and multimode fiber noise. Beamsteering noise arises when the light incident on a detector is displaced by particles in the test section [4], and vibration noise is caused by the mechanical vibrations of the test equipment. Multimode fiber noise is caused by interfering modes in the fiber coming into contact with a mode selective loss, which is discussed in detail Appendix II.

The following category of noise is detection noise, which includes Johnson noise and amplifier noise. Johnson noise occurs when any amount of voltage is applied across a resistance, and amplifier noise is produced when a weak signal is electronically amplified. The next type of noise is data acquisition noise, which includes digitization noise and bit noise. Digitization noise occurs when an analog signal is converted to a digital signal. Bit noise also arises from this process as digital data must be arranged into discrete bins. All of these noise sources were evaluated and considered during the design of the present experiment.

### 1.3 BROADBAND ULTRAVIOLET LIGHT SOURCES

A wide selection of broadband ultraviolet light sources is commercially available. Non-commercial broadband ultraviolet light sources are also achievable, but they require alignment and are more difficult to use. The sources considered for the experiment will be discussed here, beginning with the non-commercial sources. One broadband UV light source was developed at the Engine Research Center by supercontinuum generation. This involved using a pump laser at 337 nm and sending the light through a single mode UV fiber, which resulted in the generation of a broadband UV source at the output end of the fiber which is discussed in the paper in Appendix III. This light source was not chosen because the set-up for supercontinuum generation was large and the UV broadband source was not very stable compared to other sources. The next source considered was a Ti:sapphire mode-locked laser emitting 706 nm which was then sent through a doubling crystal creating 353 nm emission. The spectral bandwidth of the 353 nm source was  $\sim 4$  nm at full width half max (FWHM). This source was not chosen due to the complexity and cost of the laser and the mode-locking stability. Another UV light source in consideration was a Deuterium lamp. This is a commercially available fiber-coupled lamp that emits light from 200 to 400 nm. This lamp was not chosen because of its low spectral radiance. The following light source in consideration was a 309 nm Light Emitting Diode (LED) with a spectral bandwidth of  $\sim 26$  nm FWHM as seen in Figure 1.1. This 309 nm LED has a spectral radiance that is  $\sim 100$  times that of the fiber-coupled Deuterium lamp, which is why this UV light source was selected for the experiment.

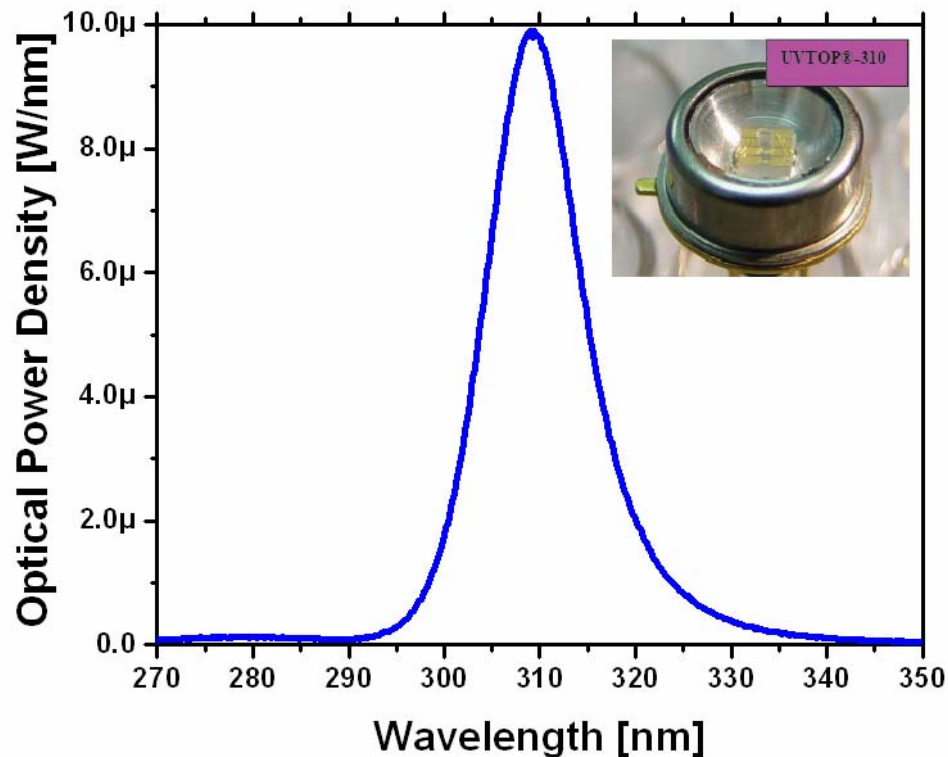


Figure 1.1 Sensor Electronic Technologies UVTOP-310 LED spectrum. Inset is a picture of the LED.

## 1.4 ULTRAVIOLET SPECTROMETERS

The next selection is the spectroscopic instrument used for analyzing the data. The first spectrometer in consideration is the grating spectrometer. The grating spectrometer is a commercially available instrument that typically results in low throughput and low resolution. The following instrument in consideration is called the Fourier Transform Ultraviolet (FTUV) spectrometer. This instrument is identical to the well-known Fourier Transform Infrared (FTIR) spectrometer in all aspects except for the wavelength measurement range. This instrument has a higher throughput and higher resolution than the grating spectrometer, but issues arise in the UV wavelength range when selecting a nano-

positioner for the moving mirror. To resolve this problem another instrumentation technique can be used called Spatial Heterodyne Spectroscopy (SHS) discussed in detail in the paper in Appendix IV. This instrumentation method was chosen because of its high throughput, high resolution, compact size, and no moving parts. Both the grating spectrometer and the SHS instrument will be considered in detail in Chapter 2.

## **CHAPTER 2. DESIGNING A BROADBAND HIGH SPEED HIGH RESOLUTION INSTRUMENT**

This chapter describes in detail the design development of the broadband high speed instrument for ultraviolet experimentation. All measurement techniques will be considered for this design and described in detail.

### **2.1 GRATING SPECTROMETER CONSIDERATIONS**

The first option for this UV experiment is to use a grating spectrometer and the selected UV LED. Since grating spectrometers are commercially available, they are easy to obtain and use. Unfortunately, there are some inherent issues that arise when trying to use a grating spectrometer for high resolution spectroscopy. The optical extent of a grating spectrometer is compared to that of the interferometer in the appendix of the literature in Appendix IV. Using Equation a9 in the text of Appendix IV, the extent of the grating spectrometer is  $\sim 700$  times lower than the interferometer; therefore the grating spectrometer was not the best option for this experiment.

#### **2.1.1 Low throughput**

Grating spectrometers typically suffer from their low throughput. In order to achieve a high resolution measurement in a grating spectrometer, the slit size on the spectrometer must be relatively small,  $\sim 20 \mu\text{m}$  for a common commercial grating spectrometer. Because of this slit size, most of the light will be lost at the input of the grating spectrometer, which is undesirable. Although the UV LED has a higher spectral radiance than the Deuterium lamp, the LED cannot be focused down to such a small slit size resulting in a loss of light at the slit.

### 2.1.2 Large instrument size for high resolution

In order to achieve a high resolution measurement with a grating spectrometer, the instrument size has to be increased. This occurs so that the input angles of the light are as small as possible allowing the user to more easily identify the measured range of wavelengths. Commercial instruments can be up to ~1 m in length resulting in higher resolution spectra.

## 2.2 FTUV INTERFEROMETER CONSIDERATIONS

The next instrument considered for measurement is the FTUV interferometer as pictured in Figure 2.1. The FTUV is a Michelson interferometer that is designed in the ultraviolet wavelength range. It uses a beamsplitter and two mirrors, one that moves, to cause the light to interfere with itself.

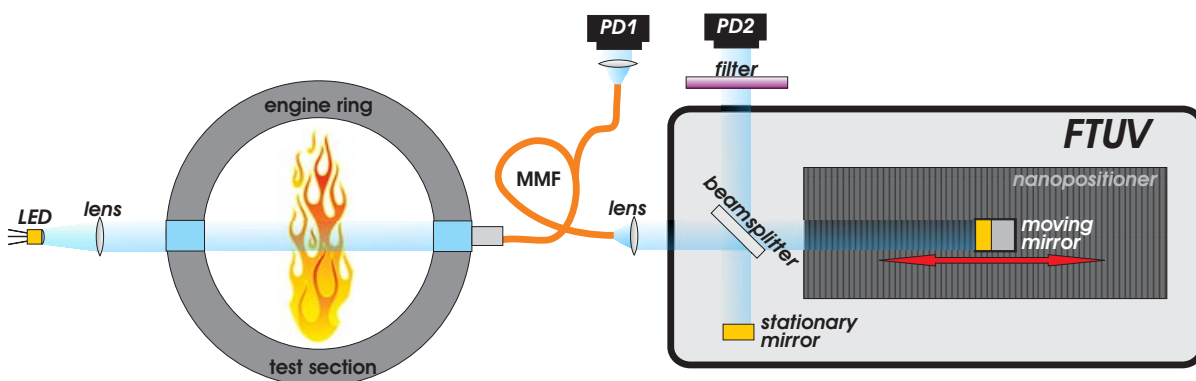


**Figure 2.1 Schematic of the FTUV interferometer arrangement. The UV LED is collimated then sent through the engine ring test section where OH absorption will occur. The light is then sent through a multimode fiber by a collimation package. The fiber is split, half of it going to photodiode 1 and the other half is collimated and travels into the FTUV instrument indicated by the gray box. As the nano-positioner moves a spectrum is recorded by photodiode 2, which is preceded by a filter to reject chemiluminescence.**

### 2.2.1 High resolution spectra

A common characteristic of FTUV, FTIR, and Michelson interferometers is that they all can achieve high resolution spectra. The following equations explain how the optical path difference relates the interferogram to the original signal [5]. The optical path difference  $t$  seconds after the zero optical path difference point is represented by:

$$\delta = 2vt \text{ [cm]}, \quad (2.1)$$

where  $v$  is the velocity of mirror movement in cm/s. Next, the recorded interferogram equation for polychromatic light is represented by:

$$I(\delta) = \int B(\nu) \cos(2\pi\nu\delta) d\nu, \quad (2.2)$$

where  $B(\nu)$  is equal to the intensity of the source signal as a function wavenumber and  $\nu$  is the wavelength measured in wavenumbers. To obtain the original spectrum from the interferogram, the following equation must be used:

$$B(\nu) = \int I(\delta) \cos(2\pi\nu\delta) d\delta. \quad (2.3)$$

An original OH spectrum convoluted with the UV LED spectrum was simulated. That spectrum was then input into a simulated interferometer to achieve the interferogram,  $I(\delta)$ . Using Equation (2.3), the original spectrum was resolved as shown in Figure 2.2. Given that the moving mirror step size is small enough and the stage travels a long distance, a high resolution broad spectrum is easily achievable. In the case of the FTUV, an appropriate nano-positioner has to be carefully selected in order to avoid excessive noise originating from the

nano-positioner movement. Infrared wavelengths are much longer than UV wavelengths, so the tolerance on the nano-positioner movement is more relaxed.

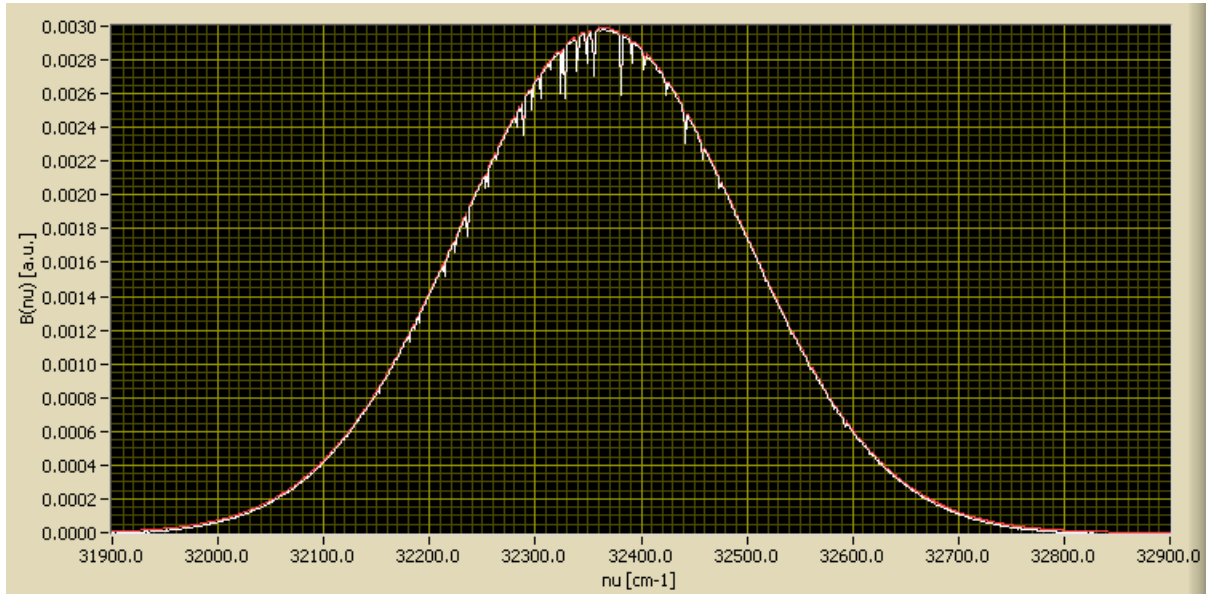


**Figure 2.2 Simulated OH spectrum convoluted with the UV LED spectrum. The white line represents the transformed  $B(\nu)$ , and the red line represents the original  $B(\nu)$ . From the graph, it is apparent that high resolution spectra are achievable given the proper equipment.**

### 2.2.2 Moving mirror issues

A nano-positioner can cause problems during data acquisition when using UV wavelengths. The pitch, yaw, and roll of the nano-positioner have to be designed for when using this type of stage in the FTUV interferometer. If the tilt of the moving mirror in any direction varies too much, it could cause problems such as reducing the fringe contrast and affecting the shorter wavelengths from a polychromatic source more than the longer wavelengths. The mirror tilt,  $\beta$ , does not degrade the fringe contrast if:



$$\beta \prec \frac{1}{20D\nu_{\max}}, \quad (2.4)$$

where  $D$  is the beam diameter and  $\nu_{\max}$  is the highest measured wavenumber [5]. This interferometer design uses a traveling mirror that moves in steps rather than a continuous motion. Because of this configuration, the accuracy of the each step must be considered. Since the instrument is to be designed for high speed and high resolution spectra, the nano-positioner must move in small steps at a fast speed and stop accurately within a few nanometers. This causes difficulties in selecting a nano-positioner since such instruments are not quite technically developed yet for this type of use.

## 2.3 HIGH SPEED SHS DESIGN

Since the grating spectrometer provided only low resolution spectra, and the FTUV interferometer has stability issues due to the moving mirror, the SHS instrument was chosen for the UV experiment. SHS provides a high throughput high resolution instrumentation method for UV experiments.

### 2.3.1 Light source and test engine selection

The UV supercontinuum was not chosen as the light source due to its complicated set-up and instability as described above. The spectral radiance of the 309 nm LED and the fiber-coupled Deuterium lamp was compared, and the UV LED provided ~100 times higher spectral radiance than the Deuterium lamp; therefore it was chosen as the light source for the UV experiment. Once the light source was chosen, a test engine had to be selected. There were a few choices including the General Motors (GM) metal engine, the GM optical engine,

and the Triptane engine. The UV LED has an aperture of 6 mm in diameter; therefore the GM metal engine would be a poor choice since the through holes in the engine head are much smaller in diameter as pictured in Figure 2.3. The GM optical engine has greater optical access, but the engine does not fire. This is a problem because OH absorption only occurs in the engine if combustion takes place, so this engine is undesirable. The Triptane engine pictured in Figure 2.4 was chosen based on the potential for the highest throughput.

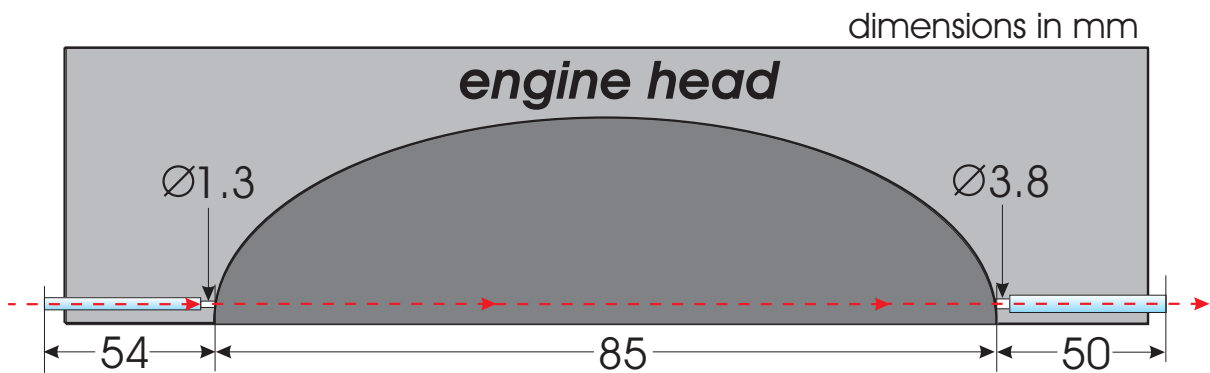


**Figure 2.3 GM metal engine schematic. The GM metal engine achieves optical access by two holes drilled directly into the engine head. The light, indicated by the red dotted line, is sent through the first smaller window into the combustion chamber then back out through the second larger window.**

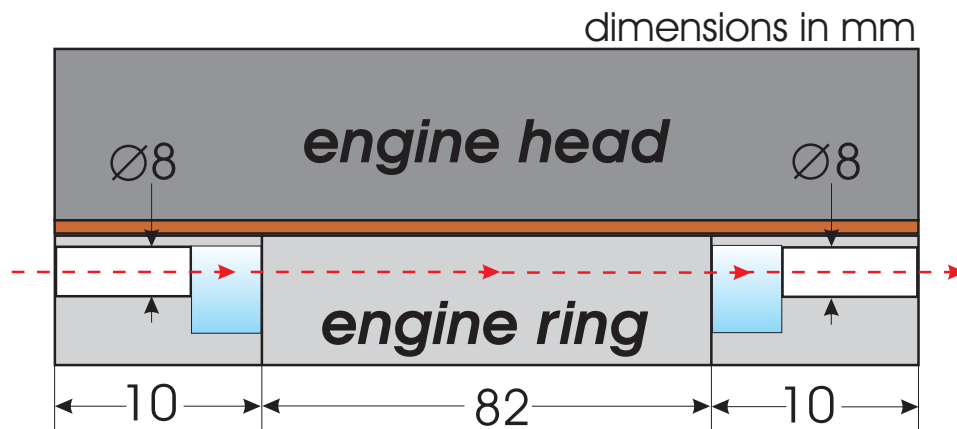


**Figure 2.4 Triptane engine schematic. The Triptane engine uses an engine ring for optical access rather than drilling holes in the engine head. The head and the ring are separated by a copper retaining ring. The light, indicated by the red dotted line, is sent through the first window into the combustion chamber then back out through the second window in the engine ring.**

### **2.3.2 SHS simulation**

Once the light source and the test engine were selected, the SHS system was simulated in MATLAB. The simulation was based on the work of Harlander et al. [6]. The simulation input parameters include the wavelength range, the diameter of the input beam, the grating grooves/mm, the number of camera pixels illuminated, and the size of each pixel. With this information, the grating 1<sup>st</sup> order Littrow angle is given as an output along with the magnification factor as seen in Figure 2.5, which has to be greater than 1 in order to avoid aliasing in the system. This simulation helps design the SHS instrument given that the camera specifications are known.

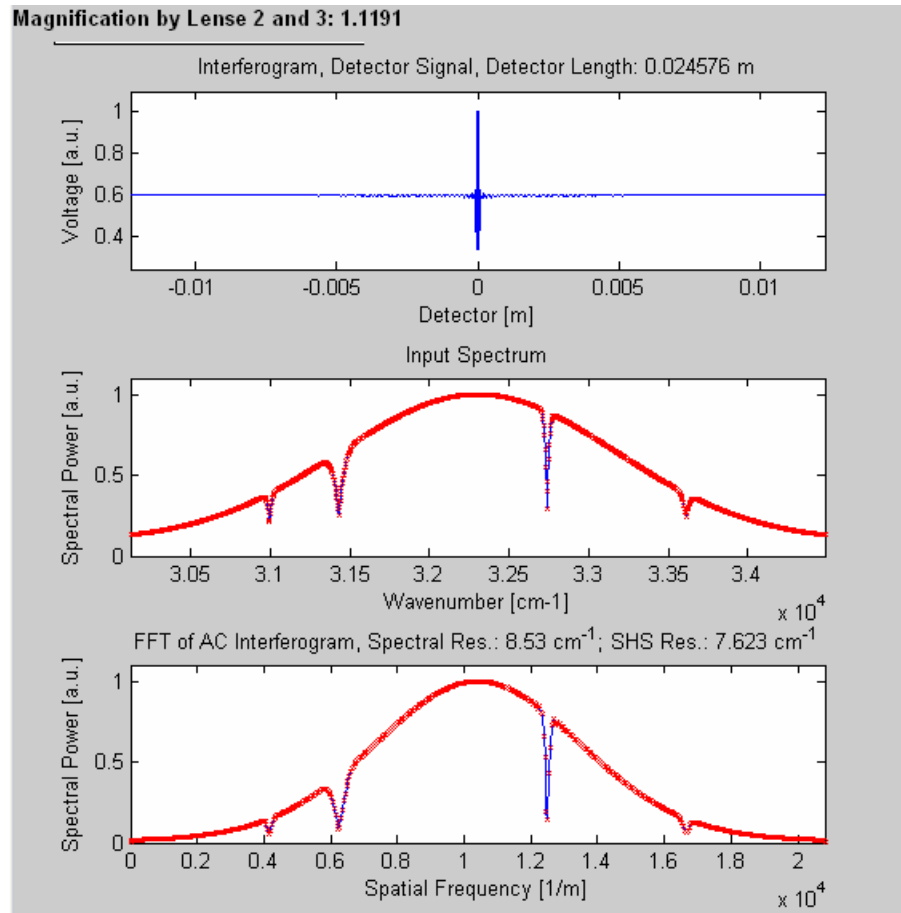


**Figure 2.5 Sample MATLAB simulation output.**

### 2.3.3 Optics selection

Once the SHS system was simulated in MATLAB, the optics had to be chosen carefully. Based on the SHS simulation, the appropriate grating was chosen for the camera used in the experiment. In the ultraviolet wavelength range, the lowest grating groove density commercially available is 110 grooves/mm. Since the simulation required only half that number of grooves, only one grating was used in combination with a precision UV mirror. In this case, the resolution of the instrument will be decreased by a factor of two allowing the grating with a higher groove density, 110 grooves/mm, to be used in place of two lower

groove density gratings that are not commercially available. The next optic that will be considered is the beamsplitter. The beamsplitter is designed for a 45 degree angle of incidence with an anti-reflection coating centered at 309 nm. For the beamsplitter, as well as the grating and mirror, the flatness has to be specified. A rule of thumb for optical flatness specification in interferometric systems is to use optics with a flatness of  $\lambda/10$  or better at the wavelength of use.

In order to image the SHS system, a set of lenses will be designed for. In this experiment there are three lenses needed to image the system as seen in Figure 2.6. The first lens needed is the input lens, which focuses the UV LED in the center of the test section, in this case, the engine ring that would be located in the Triptane engine. The second lens needed is the collimating lens, which collimates the beam at the engine ring output. This collimated beam is then sent into the SHS instrument with a very small divergence angle. After exiting the SHS instrument, another lens is needed to focus the beam down in order to eliminate higher orders with an iris before being sent to the UV camera lens for detection.

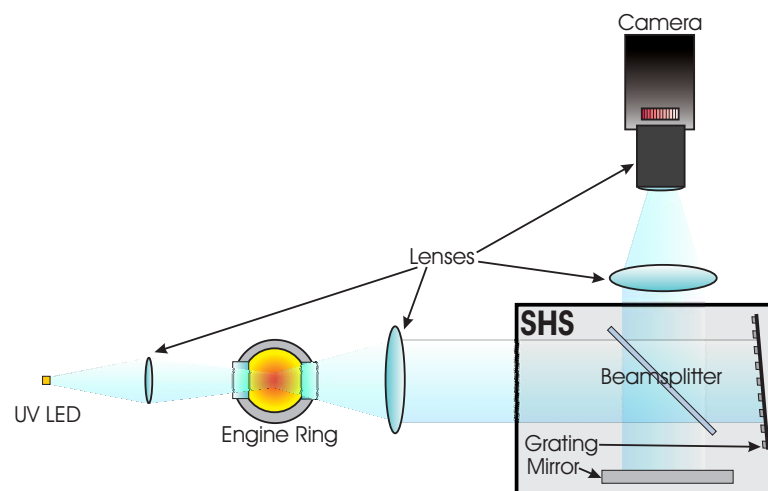


**Figure 2.6 High-speed SHS schematic.**

#### 2.3.4 Design difficulties

There were a few problems that arose during the experiment. The major issue that had to be dealt with is the wavelength dispersion in the beamsplitter. Since the beamsplitter used was  $\sim 7$  mm thick, the dispersion of the wavelengths in the glass had to be addressed. In order to avoid this problem, a compensator plate is needed to account for the extra glass thickness that one of the interferometer arms is subject to. The thicknesses of the beamsplitter and compensator plate have to match within a certain degree of accuracy. In this case, the thickness tolerance between the two plates had to be within  $\frac{1}{2}$  micron. These optics typically have to be custom manufactured, greatly increasing the SHS instrument cost. In order to avoid this cost, a thin pellicle beamsplitter was used to try to avoid the wavelength dispersion.

There are a few issues that arise when a pellicle beamsplitter is used in place of a glass beamsplitter. The pellicle is only  $\sim 2$   $\mu\text{m}$  thick and should not cause much wavelength dispersion, but the pellicle has its own intrinsic problems. Since the pellicle is so thin, it is subject to movement due to air currents, hindering any measurements. Data analysis issues arise because of the ghosting from the pellicle beamsplitter. Since the pellicle is extremely thin, the reflection from the front and back side of the pellicle may overlap causing data analysis issues when trying to locate the interferogram. This could be avoided by covering the pellicle with an anti-reflection coating on one side, but that would add to the thickness of the pellicle leading to an increase in dispersion. Therefore, the best option is to use the glass beamsplitter and compensator plate arrangement.

## **2.4 OTHER HIGH-SPEED MEASUREMENT OPTIONS**

Since SHS turned out to be more costly and difficult than expected, other high speed measurement options will be discussed and considered for future work.

### **2.4.1 Grating spectrometer for low resolution measurement**

Although trying to obtain a high resolution spectra ideally would lead to greater temperature accuracy that may not be necessary. Although SHS was a good option for acquiring high resolution spectra, a grating spectrometer might be sufficient. The SHS instrument is a great instrument for high resolution, low light applications, but its performance suffers when a broad spectra needs to be measured. A grating spectrometer may be sufficient to measure temperature although it provides low resolution.

### **CHAPTER 3. CONCLUSIONS AND FUTURE WORK**

Spatial Heterodyne Spectroscopy proved to be applicable to combustion measurements, but it may not be the best option for absorption spectroscopy. SHS is ideal for high resolution low light applications that have a narrow spectrum. This would make it an ideal application for Raman spectroscopy. Raman spectroscopy consists of illuminating a sample with a laser beam, then collecting the inelastic scattered light with a lens and sending into a spectrometer for analysis. Raman scattering inherently results in weak signals, which can be analyzed using the SHS instrument because of its high throughput advantage. Therefore the next step in UV experimentation is to use the SHS instrument for Raman spectroscopy.



## REFERENCES

- [1] Younger, Sean, 2005 "OH Absorption Spectroscopy to Investigate Light-Load HCCI Combustion," University of Wisconsin-Madison, Masters.
- [2] Walewski, J. W., Filipa, J. A., and Sanders, S. T., 2008, "Optical Beating of Polychromatic Light and its Impact on Time-Resolved Spectroscopy. Part I: Theory," *Appl. Spectrosc.* (accepted for publication).
- [3] Filipa, J. A., Walewski, J. W., and Sanders, S. T., 2008, "Optical Beating in Time-Resolved Spectroscopy. Part II: Strategies for Spectroscopic Sensing in the Presence of Optical Beating," *Appl. Spectrosc.* (accepted for publication).
- [4] Kranendonk, L. A., and Sanders, S. T., 2005, "Optical Design in Beam Steering Environments with Emphasis on Laser Transmission Measurements," *Appl. Opt.*, **44**(31), pp. 6762-6772.
- [5] Griffiths, P. R. and de Haseth, J. A., 1986, *Fourier Transform Infrared Spectrometry*, John Wiley, New York.
- [6] Harlander, J. M., Reynolds, R., and Roesler, F. L., 1992, "Spatial Heterodyne Spectroscopy for the Exploration of Diffuse Interstellar Emission Lines at Far-Ultraviolet Wavelengths," *Astrophys. J.*, **396**(2), pp. 730-40.

## APPENDIX I. MODELESS WAVELENGTH-AGILE LASER

### EXPERIMENT: *Modeless operation of a wavelength-agile laser by high-speed cavity length changes*

Laura Kranendonk, Renata Bartula, and Scott Sanders

#### I.1 ABSTRACT

An external cavity laser has been designed for rapid but stable wavelength-tuning. To enhance the tuning stability, cavity modes are suppressed by rapidly changing the cavity length as part of the wavelength scanning mechanism. The  $\sim 27$  cm cavity length is modulated at speeds up to 1190 m/s, corresponding to  $\sim 90\%$  of one wavelength in an optical round-trip time. The laser scans from 1370-1464 nm and back at a rate of 15.5 kHz with a measured instantaneous linewidth of  $\sim 0.3$  nm. This high speed modeless laser has several advantages over traditional designs which will be discussed here.

#### I.2 NOMENCLATURE

AOM: Acousto-optic modulator

ASE: Amplified spontaneous emission

$c$ : Speed of light

$\Delta f$ : Frequency shift

$\Delta L$ : Change in cavity length in one optical round trip

FSFL: Frequency-shifted feedback laser

FSR: Free spectral range

$I$ :	Transmitted intensity
$I_o$ :	Initial intensity
$L$ :	Instantaneous cavity length
$\lambda$ :	Instantaneous wavelength
$R$ :	Ratio of $\Delta L$ to $\lambda$
$\tau$ :	Optical round-trip travel time in the cavity
$V$ :	Instantaneous speed of cavity length change

### I.3 INTRODUCTION

Laser designs generally incorporate laser cavities, which in turn generally define cavity modes. The cavity modes tend to enforce lasing at specific “resonant” wavelengths. For this reason, cavity modes tend to narrow the spectral width of the laser output. Narrow spectral width is a common laser characteristic, and is considered useful in some applications, including interferometry and high-resolution spectroscopy.

Lasers that can be scanned over a broad wavelength range are becoming increasingly popular for a variety of applications [see for example, 1]. In a common tunable laser design, single-mode operation is maintained by increasing the cavity length as the laser wavelength is increased so that a fixed number of wavelengths precisely fill the cavity. In such a laser, the ratio of the total scanning range to the dynamic laser linewidth is typically  $10^7$  or more, making the laser especially useful for broadband, high-resolution spectroscopy, for example.

Unfortunately, as the tuning speed is increased, the ability to maintain precision cavity lengths and single-mode operation becomes increasingly challenging. In applications such as wavelength-agile absorption spectroscopy [2] and optical frequency-domain imaging [3],

broad wavelength scans ( $> 5\%$  of the center wavelength) in short times ( $< 50 \mu\text{s}$ ) are particularly useful. At these tuning rates, one approach is to abandon the precision cavity length adjustment and allow multimode laser operation. Example multimode lasers include [2, 4, 5]; such lasers tune by “hopping” among cavity modes. A simplified picture is as follows. A large number of laser modes (typically of order 105) exist in the laser’s tuning range. The tuning element, which is typically a vibrating or rotating mirror paired with a diffraction grating, promotes lasing among some narrow distribution of these modes at any instant. The center wavelength of the distribution is swept by the tuning element. Such multimode lasers are relatively simple to construct, and tuning speeds may be limited only by the tuning element itself. Compared to the single-mode approach, the multi-mode option presents at least three possible drawbacks. First, the output no longer actually scans in wavelength, but rather “hops” among available modes in some fashion. Second, the details of the spectral behavior of each scan are generally different, because of the stochastic distribution of laser power among available modes. Finally, the instantaneous spectral width of the output is generally broader than in the single-mode case. The novel laser design presented here attempts to resolve the first two issues above by eliminating laser modes altogether. The broader width is not resolved; the ratio of the scanning range to the laser linewidth is only  $\sim 103$ , compared to 107 in the single-mode case, and this is simply accepted, since it is sufficient for many high-speed laser scanning applications.

Reduction of mode build-up has been previously reported using frequency-shifting elements within the cavity [6, 7]. Typically, an acousto-optic modulator (AOM) is used to constantly shift the feedback frequency of the circulating light, so that a single mode no longer resonates. This approach works even for fixed-wavelength lasers; for example Lim [6]

demonstrates the linewidth broadening occurring in a fixed-wavelength laser when the AOM is turned on. Yoshizawa [7] characterizes such “frequency-shifted feedback lasers” (FSFLs) in terms of the ratio of the frequency shift ( $\Delta f$ ) encountered in one optical pass to the cavity free spectral range (FSR). We term this ratio “ $R$ ”, and below discuss the performance of our design in terms of an analogous ratio. Yoshizawa studies  $R$  ranging from 0.21-1.4; the laser discussed in this paper encompasses  $R$  values of 0-1.5.

Initially, we attempted to incorporate an AOM into our original wavelength-agile laser cavity [2] to develop a modeless, rapid-scanning laser. However, in addition to the added complexity, cost, and cavity losses, we were unable to find an AOM compatible with our wavelength-agile laser. A “broadband” AOM operating continuously throughout the  $\sim 100$  nm scanning range of our laser was not available; neither were AOMs that could be scanned rapidly enough to track our scanning wavelength. Fortunately, we discovered an alternative: rather than using an AOM to shift the feedback wavelength, we modulated the cavity length itself to prevent resonance among cavity modes. Note that this means the photons in our cavity gain inconsequential momentum relative to the photons passing through a typical AOM; the photons are essentially unaltered and it is only the cavity that changes. Cavity length modulation is a natural adaptation to a rapid-wavelength-scanning laser architecture, as we show below. Like FSFLs, our laser can be characterized by an  $R$  value. Below we describe our “modeless” laser, its benefits and potential applications.

## **I.4 LASER DESIGN**

Based on the need for a wavelength-agile laser cavity with well-behaved wavelength tuning, a new “modeless” laser configuration was developed. The design was first optimized using a

computer animation, the details of which are provided in the next section. The actual laser was then assembled and tested to confirm the predicted results.

#### **I.4.1 Computer animation**

Before the laser was constructed, the configuration and specifications were optimized using a computer simulation. The simulation was facilitated by an imaging program (Persistence of Vision – Ray Tracer, ‘POV-Ray’) used to animate the path of the light as well as calculate the instantaneous lasing wavelength and theoretical spectral resolution. The code modeled the inputs as grating grooves per millimeter, beam diameter, grating angle, and other cavity geometries. Cavities employing both single (Fig. 1) and double (Fig. 2) passes off the grating were studied. The factors used to determine the optimal set-up were the spectral resolution, maximum speed of the cavity length change ( $V_{max}$ ), maximum  $R$ , total cavity length, and ease of construction. A summary of representative simulation results are shown in Table 1. For our typical application [2], high resolution is desirable for monitoring gas absorption features, particularly at low pressure. Short cavity lengths are desired to facilitate rapid scanning: if the cavity is too long, there are too few optical round trips before the spectrum fed back from the grating changes appreciably, and the laser performance degrades (see discussion section). High cavity speed is desired to for increased suppression of laser modes. Designs involving a double-pass off the grating (defining the end of the cavity with a mirror after the grating rather than the grating itself, as shown in Fig. 2) were rejected because of marginal improvement in spectral resolution for the increased complexity, as well as longer total cavity lengths. The single pass geometry (Fig. 1) was therefore chosen because it represented the simplest version that met our needs.

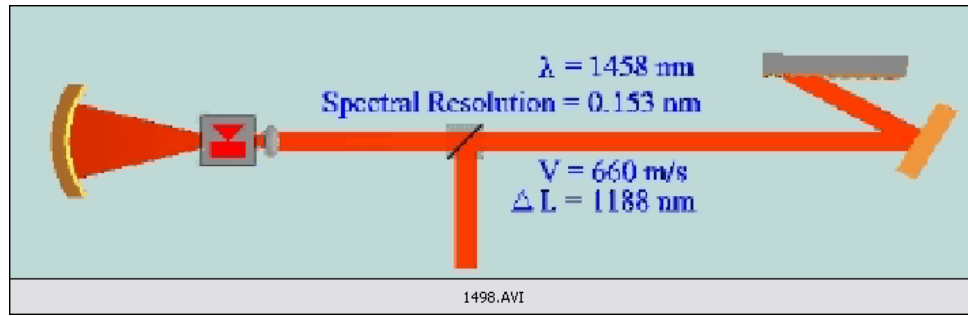


**Fig. 1. (0.411 MB),** Movie of the new single pass wavelength agile, modeless, external cavity diode laser described in this paper. The animation includes instantaneous cavity speed ( $V$ ), change in cavity length in an optical round trip ( $\Delta L$ ), spectral resolution, and wavelength ( $\lambda$ ) values using a 1200 grooves/mm grating.

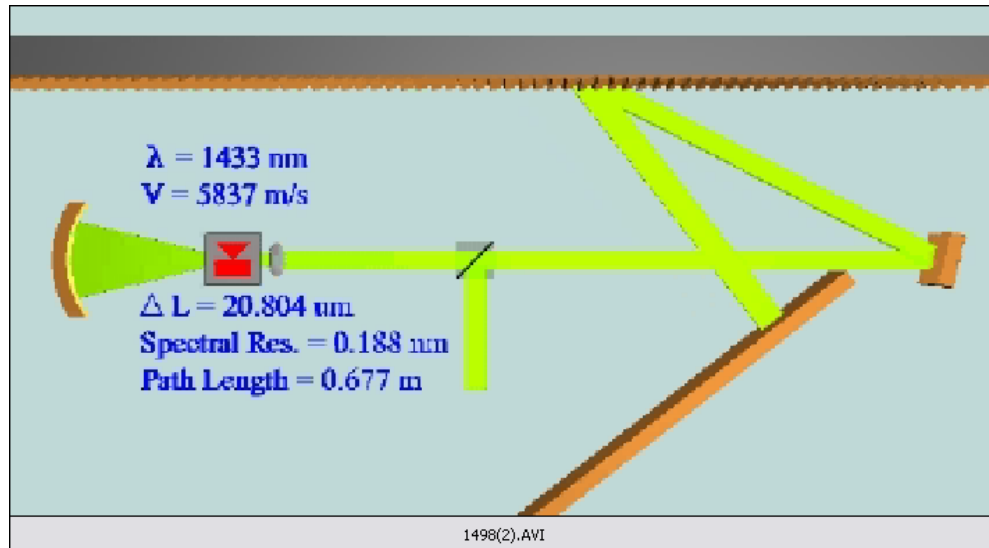


**Fig. 2. (0.765 MB),** Movie of a novel double pass external cavity diode laser design with instantaneous cavity speed ( $V$ ), change in cavity length in an optical round trip ( $\Delta L$ ), spectral resolution, wavelength ( $\lambda$ ), and total path length using a 1050 grooves/mm grating.

**Table 1.** Results from computer simulations, where single pass geometry is shown in Fig. 1, and double pass is shown in Fig. 2.

Grating Passes	Available Grating [grooves/mm]	Spectral Resolution (max) [nm]	$V_{max}$ [m/s]	$R_{max}$	Path Length (ave.) [m]	Grating Width [cm]
Single	1200	0.287	1,190	1.50	0.27	2
Single	1050	0.429	527	0.67	0.27	2
Single	950	0.501	397	0.50	0.27	2
Single	750	0.661	185	0.24	0.27	2
Double	1200	0.136	103,000	858	1.48	90
Double	1050	0.188	5,873	14.8	0.63	9
Double	950	0.228	3,553	8.27	0.59	5
Double	750	0.314	1,122	2.24	0.57	2

#### I.4.2 Laser construction

The details of the final (single pass) design shown in Fig. 1 are as follows. A broadband semiconductor pump chip (developed at the Ahura Corp., part number 102D) was used as the gain element. This element was angle-faceted to eliminate the possibility of forming additional cavities within our designed cavity. A high quality spherical mirror (Optosigma 035-0150,  $\lambda/4$  sphericity) formed one end of the laser cavity. However, this spherical mirror was only  $\sim 10\%$  efficient in coupling light back into the semiconductor waveguide, thus in future designs we are pursuing angle-flat chips with the flat surface defining this end of the cavity. The gain element was mounted in a fixed location. The spherical mirror and lens were each mounted on high-sensitivity XYZ stages (Thorlabs MDT616). The collimated light was directed at the resonant scanner (Electro-Optical Systems, Inc, SC30, 3mm x 3mm plane mirror, 15.54 kHz resonant frequency), set on a four-axis stage (New Focus 9071). The amplitude of the mirror oscillation was adjustable, but the frequency was not. The light from the vibrating mirror was then directed at the plane ruled diffraction grating (Edmund Scientific, NT55-263, 1200 g/mm), mounted on a kinematic mount that allowed for rotation of the grating grooves (New Focus 9481). A 50:50 beamsplitter cube (Edmund Scientific



R47-235) was used to extract the laser beam. Two beams emerge from the cube, but we only use the one shown, because the other one could be contaminated by amplified spontaneous emission (ASE) that is not rejected by the grating. Note that light also leaks out the cavity from the zero<sup>th</sup>-order diffraction from the grating, but in addition to possible ASE contamination, this light scans in space and is therefore not easily usable. The beam extracted at the beamsplitter cube is coupled into a single-mode fiber for delivery to the end-use.

The average cavity length ( $L$ ) was 0.27 m, corresponding to a free spectral range of 553 MHz. The average output power was 5 mW, and the measured instantaneous linewidth was 0.3 nm, determined by comparing a measured and simulated atmospheric-pressure H<sub>2</sub>O vapor spectra. Note that the measured linewidth is approximately 1.3 times larger than the calculated spectral resolution, possibly because of imperfect alignment of the beam in the cavity.

#### **I.4.3 Modeless operation**

The primary goal for the present laser design is to eliminate the effect of cavity modes. In a fashion analogous to FSFLs, this occurs in our laser by rapidly modulating the cavity length to prevent resonance of preferential wavelengths within the cavity. Because of the arrangement of the grating shown in Fig. 1, the wavelength scanning is accompanied by cavity length change. The speed ( $V$ ) reported in the animation is the instantaneous time derivative of the cavity length. Because the mirror vibrates sinusoidally,  $V$  varies in an approximately sinusoidal fashion as well. Figure 1 also shows  $\Delta L$ , the instantaneous change in cavity path length occurring in the optical round-trip time ( $\tau$ ). The ratio of  $\Delta L$  to the wavelength, termed  $R$  in this paper, is an important parameter because it governs the suppression of laser modes. With  $R \approx 0$ , the laser behaves as an ordinary multimode tunable

laser. The  $R$  we use here is analogous to the ratio used in AOM-based modeless lasers. In reference [7], the ratio is defined in terms of the frequency shift of light occurring in one round trip due to the AOM,  $\Delta f$ , and the cavity free spectral range (FSR) as

If we imagine that the acoustic waves in the AOM were truly decreasing the cavity length at speed  $V$ , then we could express  $\Delta f$  as

$$R = \frac{\Delta f}{FSR} \quad (1)$$

If we imagine that the acoustic waves in the AOM were truly decreasing the cavity length at speed  $V$ , then we could express  $\Delta f$  as

$$\Delta f = \frac{V}{c} f = \frac{V}{\lambda} = \frac{\Delta L}{\tau \lambda} = \frac{\Delta L \cdot c}{2L\lambda} \quad (2)$$

and thus  $R$  as

$$R = \frac{\Delta f}{FSR} = \frac{\Delta L c / 2L\lambda}{c / 2L} = \frac{\Delta L}{\lambda} \quad (3)$$

Thus the AOM and variable-length cavity, though different means of eliminating laser modes, can be characterized by analogous  $R$  values.

Figure 3 illustrates several important features of our laser. The bottom panel presents the output power versus time for the laser shown in Fig. 1. The large variation during tuning shown on the bottom panel of Fig. 3 is an effect of the finite bandwidth of the gain element. The maximum gain of the element occurs roughly at 1430 nm, and there is simply less gain at the endpoints of the scan. The maximum change in cavity length speed is 1190 m/s, corresponding to  $\Delta L$  of 2.1  $\mu\text{m}$ , an  $R$  of 1.5, and  $\lambda_1$ - $\lambda_2$  from 1370-1464 nm.  $R$  passes through zero at the edges of the scan because of the sinusoidal motion, but in the bottom panel,

transition to ordinary multimode behavior is not observed. The middle panel shows that when the mirror vibration amplitude is decreased ( $\lambda_1 - \lambda_2 = 1398 - 1441$  nm) slowing the maximum  $V$  to 587 m/s, evidence of cavity modes are occasionally seen at the extremes of the scans, where  $R$  passes through zero. Finally, the top graph shows a very slow change in cavity length ( $V_{max} = 13.6$  m/s,  $\lambda_1 - \lambda_2 = 1418.5 - 1419.5$  nm). Here, the laser scan is strongly affected by laser modes. The laser exhibits a stronger and cleaner signal when cavity modes prevail. Although the “modeless” operation is “noisier”, it is preferred because of the spectral behavior during the scan. Based on the results shown in Fig. 3, we estimate that when  $R \approx 0.05$  or lower, it is possible for the laser to develop cavity modes.

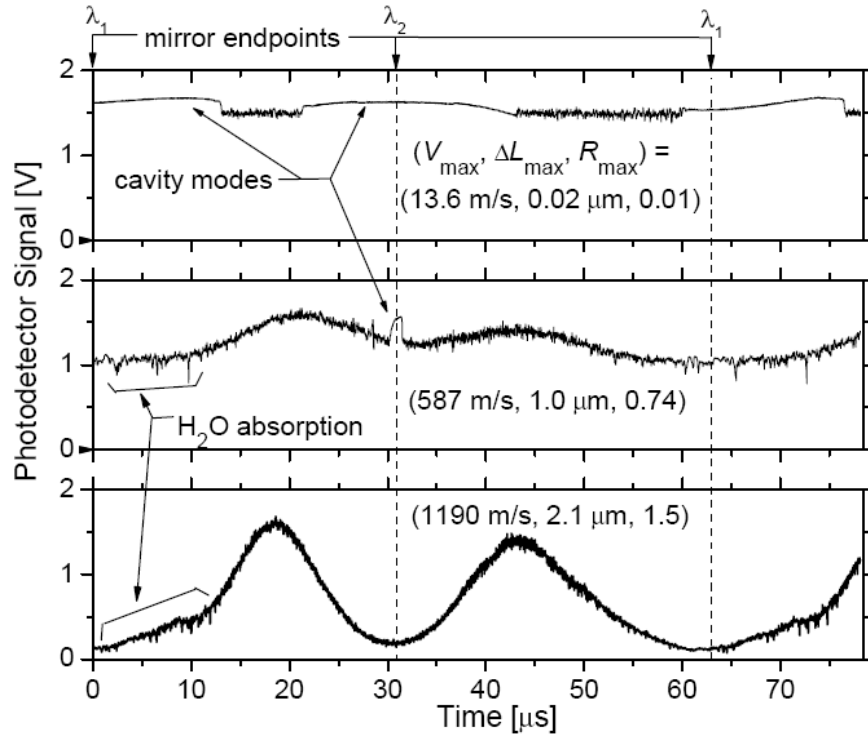


**Fig. 3 - Elimination of cavity modes.** The bottom panel is the laser signal as set up for Fig. 1 ( $\lambda_1 - \lambda_2$  is 1370-1464 nm). The middle panel shows a slower mirror oscillation, with  $\lambda_1 - \lambda_2 = 1398 - 1441$  nm. Finally, the top panel shows a very slow change in cavity length, and the cavity mode effect ( $\lambda_1 - \lambda_2 = 1418.5 - 1419.5$ ). Corresponding  $V_{max}$ ,  $\Delta L_{max}$  and  $R_{max}$  values are given.

Careful examination of Fig. 3 reveals some non-ideal aspects of the laser performance. First, there is the intensity noise during the scan, as mentioned above. Second, the intra-cavity water absorption features visible in Fig. 3 are not symmetric in blue-to-red and red-to blue scan directions. We believe both of these issues are associated with fiber-coupling the laser light extracted from the cavity. If a large multimode fiber is used, rather than the single-mode fiber used to collect the data shown in Fig. 3, these issues disappear. Therefore we believe the circulating beam contains multiple spatial modes. We expect that using a single-mode fiber coupler rather than a beamsplitter cube to extract light from the cavity would force the circulating light to be single-mode at the extraction point and therefore improve the situation. An alternative would be to simply use multimode fiber to deliver the extracted light to the end use; however, our application suffers from a “fiber mode noise” in this configuration [2]. Therefore, our present solution is to couple into a single-mode fiber and correct for the intensity noise with a reference detector; this approach works well in our application as described in section 3.

## **1.5 SAMPLE RESULTS**

A H<sub>2</sub>O vapor spectrum was measured in a high pressure (7 bar), room temperature cell, with ~0.63% mole fraction concentration of water vapor. A high pressure was chosen because our interest in combustion applications are typically high pressure [2], and because the spectral resolution of the laser is appropriate for the broad features characteristic of high-pressure spectra. The raw data is shown in Fig. 4. This data is obtained as follows. The fiber-coupled light from the laser cavity is separated using a 90/10 fiber splitter, such that 90% of the light is directed through the high pressure cell, and 10% is coupled directly to a reference

photodetector ( $I_o$ ). The light directed through the test cell is then coupled into a 62.5 $\mu\text{m}$  multimode fiber which is connected to a separate photodetector ( $I$ ). A single-mode coupler in the path through the cell was decoupled to balance the signal powers. Care was taken to balance the length of the light paths leading to the  $I$  and  $I_o$  photodetectors so that the signals were synchronized.

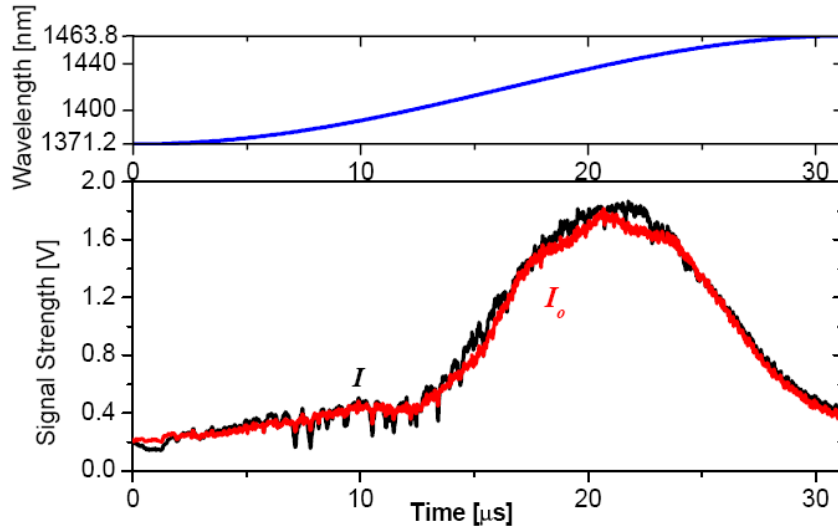


**Fig. 4 - Raw data signals taken from a high pressure (7 bar) cell at room temperature.  $I$  is the signal recorded after the cell, and  $I_o$  is the signal directly out of the laser. A fiber splitter was used to record  $I$  and  $I_o$  simultaneously.**

Figure 4 can be converted into an absorption spectrum (Fig. 5) by using Beer's Law and a baseline fit as described in [8, 9], and converting time into wavelength based on the sinusoidal mirror motion. The measured absorption spectrum is compared to a simulated spectrum from the HITEMP database [10] in Fig. 5. In a typical absorption spectroscopy application, measured spectra would be compared to a library of simulated spectra to infer the properties (e.g. gas temperature and species mole fractions) of the material under test.

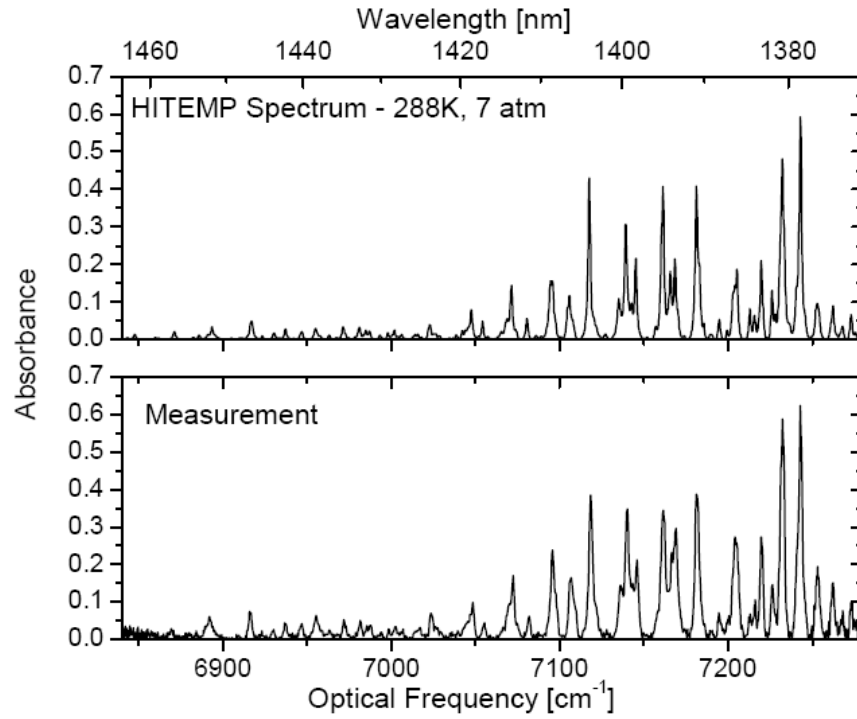


**Fig. 5 - A sample water spectrum measured in a high pressure cell at room temperature. The top panel shows the corresponding spectrum generated from the HITEMP database.**

## I.6 DISCUSSION

In this paper the cavity length changes by as much as 150% of the wavelength in an optical round trip ( $R = 0-1.5$ ).  $R$  can be adjusted in future designs in many ways. For example, a simple lengthening of the cavity increases  $R$  (by increasing the round trip optical travel time, thus increasing  $\Delta L$ ). However, in lengthening the cavity, care must be taken to ensure that the wavelength tuning does not “outrun” the laser dynamics. For example, in the design presented here, the maximum tuning speed is 0.0046 nm/ns. The optical round trip time is  $\sim 1.8$  ns. Thus the maximum wavelength tuning increment in a round trip is  $\sim 0.008$  nm. This is about 1/26 of the calculated spectral resolution at the fastest part of the scan (0.2 nm). Thus the presence of a given wavelength must grow and decay in the cavity in  $\sim 26$  round trips. In

the present laser, the round-trip small-signal gain associated with the semiconductor is  $\sim 106$ , which is high enough to support the aforementioned growth and decay. However, with lower gain or longer cavities it is easy to depart from this “quasi-steady” lasing regime, resulting in more complicated and presumably less stable tuning dynamics. Fortunately, there are other ways to change  $R$  if desired. Unlike the frequency shift associated with an AOM, the cavity length changes here can be easily varied with cavity geometry. For example, achievement of much larger  $R$  values (say  $R \sim 10$ ), or achievement of similar  $R$  values in a shorter cavity, should be straightforward. By increasing the size of the grating and the distance from the grating to the scanning mirror, the effective cavity speed can be dramatically increased.

The laser presented in this paper tunes at a maximum rate of  $4.6 \text{ nm}/\mu\text{s}$ , corresponding to a wavelength change of  $0.3\%$  per microsecond. This tuning rate represents an approximate upper limit using available resonant scanning mirrors. However, other wavelength-agile sources with significantly higher tuning rates have been demonstrated. For example, sources based on dispersion of broadband pulses have achieved tuning rates of  $\sim 40\%$  per microsecond [11] up to  $0.7\%$  per nanosecond [12]. The latter is roughly 1000 times faster than the laser presented here.

Because the laser output is modeless, it is of random phase, in contrast with traditional laser output. This feature may also be of use in some applications. For example, in some imaging applications, an undesirable “speckle” is caused by the phase coherence of the illuminating laser. If the laser described in this paper were used for imaging, we expect that such speckle would be reduced or eliminated.

## **I.7 CONCLUSIONS**

We have introduced a swept-wavelength laser that features mode-free spectral output. The longitudinal cavity modes are suppressed by rapid cavity length changes that accompany the rapid wavelength scans. The modeless nature permits continuous wavelength scans with reliable instantaneous spectral structure. The laser was designed for high-speed absorption spectroscopy but may be useful in many other high-speed measurement applications as well. The cavity design should be transferable to other types of lasers, such as external-cavity dye lasers. Compared with previous external-cavity laser designs based on precision length adjustment or AOMs, the cavity-length modulation approach described here is relatively simple and cost-effective.

## **I.8 ACKNOWLEDGEMENTS**

The authors thank Joachim Walewski for his insight and help throughout the construction of this paper. This material is based upon work supported by the National Science Foundation under Grant Nos. CTS-0238633 and CTS-0307455. The semiconductor gain element used in this work was provided by the Photonics Technology Access Program which is funded by the National Science Foundation and the Defense Advanced Research Projects Agency.

## **I.9 REFERENCES AND LINKS**

1. Wippich, M., Dessau, K.L., "Tunable lasers enhance fiber sensors," *Laser Focus World* **39**, 89-94 (2003).



2. Kranendonk, L.A., Walewski, J.W., Tongwoo, K., and Sanders, S.T., "Wavelength-agile sensor applied for HCCI engine measurements," in *Proceedings of 30th International Symposium on Combustion*, (Elsevier, Chicago, IL, 2004), pp. 1619-1627.
3. Yun, S.H., Tearney, J.F., de Boer, J.F., Iftimia, N., and Bouma, B.E., "High-speed optical frequency-domain imaging," *Opt Express* **11**, 2953-2963 (2003), <http://www.opticsexpress.org/abstract.cfm?URI=OPEX-11-22-2953>.
4. Yun, S.H., Boudoux, C., Tearney, G.J., and Bouma, B.E., "High-speed wavelength-swept semiconductor laser with a polygon-scanner-based wavelength filter," *Opt. Lett.* **28**, 1981-1983 (2003).
5. Pilgrim, J.S., "Wavelength agile external cavity diode laser for trace gas detection," *Trends Opt. Photonics* **69**, (2002).
6. Lim, M.J., Sukenik, C.I., Stievater, T.H., Bucksbaum, P.H., and Conti, R.S., "Improved design of a frequencyshifted feedback diode laser for optical pumping at high magnetic field," *Opt. Commun.* **147**, 99-102 (1998).
7. Yoshizawa, A., and Tsuchida, H., "Chirped-comb generation in frequency-shifted feedback laser diodes with a large frequency shift," *Opt. Commun.* **155**, 51-54 (1998).
8. Kranendonk, L.A., Caswell, A.W., Myers, A.M., Sanders, S.T., "Wavelength-agile laser sensors for measuring gas properties in engines," SAE Paper 2003-01-1116.
9. Wang, J., Sanders, S.T., Jeffries, J.B., Hanson, R.K., "Oxygen measurements at high pressures using vertical cavity surface-emitting lasers," *Appl. Phys. B* **72**, 865 (2001).
10. Rothman, L.S., Jacquemart, D., Barbe, A., Benner, D.C., Birk, M., Brown, L.R., Carleer, M.R., Chackerian, Jr, C., Chance, K., Coudert, L.H., Dana, V., Devi, V.M., Flaud, J.M., Gamache, R.R., Goldman, A., Hartmann, J.M., Jucks, K.W., Maki, A.G., Mandin, J.Y.,

Massie, S.T., Orphal, J., Perrin, A., Rinsland, C.P., Smith, M.A.H., Tennyson, J., Tolchenov, R.N., Toth, R.A., Vander Auwera, J., Varanasi, P., Wagner, G., "The HITRAN 2004 Molecular Spectroscopic Database," J. Quant. Spectrosc. Radiat. Transfer (to be published).

11. Walewski, J.W., Sanders, S.T., "High-resolution wavelength-agile laser source based on pulsed supercontinua," Appl. Phys. B **79**, 415-418 (2004).
12. Sanders, S.T., "Wavelength-agile fiber laser using group-velocity dispersion of pulsed super-continua and application to broadband absorption spectroscopy," Appl. Phys. B **75**, 799-802 (2002).

## APPENDIX II. MULTIMODE FIBER NOISE EXPERIMENT:

### *Estimation of signal noise induced by multimode optical fibers*

Renata Bartula and Scott Sanders

#### II.1 ABSTRACT

Optical systems involving multimode fiber generally suffer from increased noise. The noise is present whenever nonuniform optical surfaces follow the multimode fiber, provided the fiber and the conditions of the input radiation are not perfectly stable. We have demonstrated fiber mode noise in an optical spectrum analyzer measurement, and developed a simple algorithm to predict the amplitude of this noise, based on the transmission properties of the nonuniform optical surfaces. The algorithm can be useful in estimating the overall signal-to-noise ratio in optical systems; it is particularly useful for designing spectroscopic sensors.

#### II.2 NOMENCLATURE AND VARIABLES

$A_{beam}$ : area of the beam [ $L^2$ ]

$A_{speckle}$ : area of the speckle [ $L^2$ ]

$D$ : size of the beam [ $L$ ]

$E$ : electric field [ $ML/T^2e^{-}$ ]

$f_{perfect}$  fraction of the detector that is perfect (equivalent to  $p$  and  $x_C/D$ ) [1]

$J_t$ : electric field energy [ $ML^2/T^2$ ]

$L$ :	distance from fiber face to measurement position [L]
$l$ :	index of a mode [1]
$\lambda$ :	wavelength [L]
$\mu$ :	mean signal [speckles]
$\mu'$ :	mean signal with transmission term [speckles]
$MMF$ :	multimode fiber
$NA$ :	numerical aperture [1]
$N_{speckles}$ :	number of speckles [speckles]
$OSA$ :	optical spectrum analyzer
$p$ :	probability for success [1]
$p'$ :	probability for success with transmission term [1]
$q$ :	probability for failure [1]
$QTH$ :	quartz tungsten halogen
$r$ :	fiber radius [L]
$r_{aperture}$ :	radius of the aperture [L]
$r_{beam}$ :	radius of the beam [L]
$r_o$ :	radius of the fiber core [L]

$r_{speckle}$ :	radius of the speckle [L]
$\sigma$ :	standard deviation [speckles]
$\sigma'$ :	standard deviation with transmission term [speckles]
$SMF$ :	single mode fiber
$T$ :	transmission [1]
$u$ :	eigenvalue of a mode [ML/T <sup>2</sup> e-]
$V$ :	normalized frequency [1]
$x_C$	size of the unobstructed beam [L]
$z$ :	fiber optical axis [L]

### II.3 INTRODUCTION

Our research group develops and uses optical sensors for measurements of gas properties. In this process, we consider all sources of noise and try to minimize them in order to optimize sensor performance. We begin this paper by demonstrating fiber mode noise in a measurement made with an optical spectrum analyzer (OSA). Then, we develop equations that can be used to estimate the mode noise induced by using a multimode fiber in an optical experiment. Mode noise was originally discovered in 1978 by Epworth [1] and analyzed by Hill in 1980 [2]. Our analysis differs from that of Hill because we allow the nonuniform optical surfaces downstream of the multimode fiber to have finite transmission, as is common

in sensor applications. MMF noise has been studied for years since it was first discovered; therefore the basic concepts of MMF noise are well-known [3], [4].

Multimode fibers are characterized by large core diameters and/or high numerical apertures. Specifically, fibers with  $V > 2.405$  are multimode, where  $V$  is given by:

$$V = \frac{2\pi r_o}{\lambda} \times NA \geq 2.405, \quad (1)$$

and  $r_o$  is the radius of the fiber core,  $\lambda$  is the wavelength of light in the fiber, and  $NA$  is the numerical aperture of the fiber [5]. Cases with  $V$  slightly greater than 2.405 (up to perhaps 24) are termed ‘few-mode’ fibers, and cases with  $V$  much larger than 2.405 (perhaps 240 and above) are termed ‘highly multimode’. In this paper we treat only the ‘highly multimode’ case. When light is sent through a multimode fiber, it induces irregular distributions of intensity over space, both within the fiber and in the far field. For the ‘highly multimode’ situation, the intensity distribution within the fiber has strong, seemingly random variations that appear as speckles. These speckles move in space due to changes in parameters such as input wavelength, launch conditions, and fiber orientation. When the fiber output is projected onto a photoreceiver, motion of the speckles can induce noise. For example, if the photoreceiver has a nonuniform response over its active area, noise associated with motion of the speckles can mask signals one seeks to quantify. Non-uniform response of a photoreceiver is one mechanism for mode-selective loss. Other mechanisms for mode-selective losses include dirt on a window or partial clipping of the fiber output. Anytime modes are subject to mode-selective losses in a MMF, noise is induced.

In Fig. 1 we demonstrate a complex multimode fiber noise problem by comparing absorption spectroscopy results obtained using multimode and single mode fibers. This problem is more complex than the MMF problem that we will simulate in this paper because it includes many factors that are not yet well understood numerically such as spectral averaging. We will use this problem exclusively as an example of multimode fiber noise. A 20 W quartz tungsten halogen (QTH) lamp (e.g., Oriel 6319) is the light source used in the fiber comparison. The QTH lamp covers a spectral range of about 300 to 2400 nm with a peak around 900 nm, but here we look only at the output in the 1350-1420 nm range, to observe absorption from ambient water vapor (neither the lamp housing nor the optical spectrum analyzer are purged). The light from the QTH lamp was imaged onto the fiber using a high NA lens (Thorlabs LB1761,  $D = 25.4$  mm,  $f = 25.4$  mm) for one-to-one imaging. Both the multimode fiber (MMF) and the single mode fiber (SMF) were used to transmit the light to an OSA. The output from the OSA (e.g., Agilent 86142B) is shown in Fig. 1. The results were measured using a resolution of 0.06 nm, collecting 8750 points over the wavelength range shown. The sensitivity was set to -93.98 dBm. The optical input to the OSA is a short SMF patch cord; therefore we were coupling either SMF or MMF to the SMF in the OSA. In the latter case, the MMF-to-SMF coupling at the OSA input represents the mode-selective loss. The MMF noise is apparent although spectral averaging is present (the OSA spectral resolution is finite at 0.06), and temporal averaging is present (the OSA took 2 hours to record the spectrum owing to the low light levels, and the MMF was in the path of strong air currents which moved it and sampled many speckle patterns for each recorded data point).

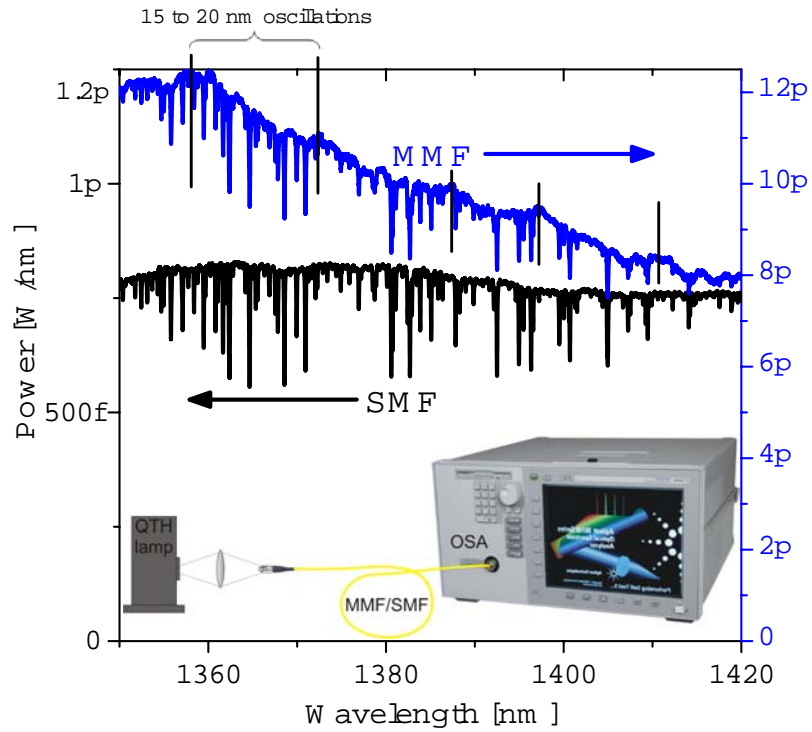


**Fig. 1. Comparison of lamp spectra measured using SMF and MMF. H<sub>2</sub>O absorption features are present in this wavelength range. The experimental schematic is inset.**

Although this spectrometer was designed for use with SMF, there are others designed for use with MMF (e.g., Ando AQ6315 and Ocean Optics USB-4000), which also exhibit considerable mode noise in similar tests. In our experience, it is a common misconception that commercial spectrometers with a MMF input do not exhibit MMF noise. In fact, there will always be some MMF noise caused by the non-uniform surfaces following the MMF. It is extremely difficult for manufacturers to make all optical surfaces uniform downstream of the MMF.

Both traces in Fig. 1 exhibit sharp absorption features due to H<sub>2</sub>O vapor. By comparing the two y-axes, it is apparent that the MMF ultimately delivers about 10 times the radiation to the



OSA. Increased signal is a common characteristic of multimode fibers and is the primary reason one often selects a MMF instead of a SMF. SMF systems are often used when their throughput is sufficient because of the virtues illustrated in Fig. 1. One can see that the output from the SMF has a flat spectrum with virtually no oscillations when compared to the MMF case. In particular, the SMF case lacks oscillations with a period of 10-15 nm that are present in the MMF case. The lack of oscillations is the primary virtue of SMF in absorption spectroscopy. The overall decreasing trend of the MMF with wavelength is not especially problematic, and is not especially common in such experiments. However, the oscillations are often problematic and are a common signature of MMF. The oscillations can mask absorption features or otherwise complicate data analysis. In our group's work in absorption spectroscopy, multimode fiber noise is an important consideration anytime multimode fiber is used. The noise affects the signal-to-noise ratio of the overall experiment so it is a key design parameter. In this paper, we develop a simple algorithm for estimating the amplitude of this noise. In future papers we hope to develop more detailed calculations of mode noise, including extension to the 'few-mode' case and the short fiber case. We also hope to treat the effect of spectral resolution in experiments using broadband light.

## **II.4 SIMULATION DEVELOPMENT**

Several assumptions are made preceding the simulation. First, we assume a fully-filled mode condition. This requires the multimode fiber to have a sufficient combination of long length and microbending so that the full numerical aperture and core diameter of the fiber have been filled by the time the mode selective loss element is reached. Strictly, the fully-filled mode condition may only be achieved if several kilometers of fiber or a mode scrambler (e.g.,

Newport FM-1) is used, but the condition is approximated in short fibers (e.g., 10 m) in many cases (e.g., if the microbending is high). The algorithm will generally overestimate the noise for very short (e.g., 1 cm) fiber lengths. The algorithm is appropriate for estimating analog signal noise in the ‘highly multimode’ case, as described above. This case is ensured when  $V \gg 2.405$  as seen in Equation (1), and causes the output radiation from the MMF to be composed of numerous speckles. Further, we assume each speckle is infinitely small; this assumption is discussed below.

We further assume that monochromatic radiation from a step-index multimode fiber is incident upon a large, perfect detector of any shape. By monochromatic we mean that the coherence time of the light source is assumed to be much larger than the pulse broadening time of the fiber. This assumption ensures that the speckle pattern at the output end of the fiber is stationary as long as the fiber and the source coupling to the fiber remain undisturbed [2]. We also assume that there is no spectral averaging since the light source is monochromatic. The detector is assumed to be large enough to at least circumscribe the incident radiation pattern, and the detector responsivity is assumed to be perfectly uniform. Next, we add a source of obscuration to the problem, represented by the gray box in Fig. 2a. The gray box is initially assumed to be completely opaque. Such clipping can occur in practical problems. For example, in our research on absorption spectroscopy in piston engines [6], the piston can clip the beam in the fashion pictured in Fig. 2a. As another example, a beam can be incident on rows of pixels where the interfaces between rows can behave like the edge shown in Fig. 2a. In the presence of such clipping, we wish to determine how much detector noise is observed as speckles move on and off the obscuration edge. Note that at this point we have posed a one-dimensional problem, as illustrated by Fig.

2b. To solve the one-dimensional problem, we must know the number of speckles that compose the multimode beam in the far field. The number of speckles is solved for by the

following equation:  $N_{\text{speckles}} = \frac{1}{2} \frac{A_{\text{beam}}}{A_{\text{speckle}}} = \frac{1}{2} \frac{\pi r_{\text{beam}}^2}{\pi r_{\text{speckle}}^2} = 2 \left( \frac{r_o \times NA}{\lambda} \right)^2$ , which is derived as Equation

(A11) in Appendix I of the text.

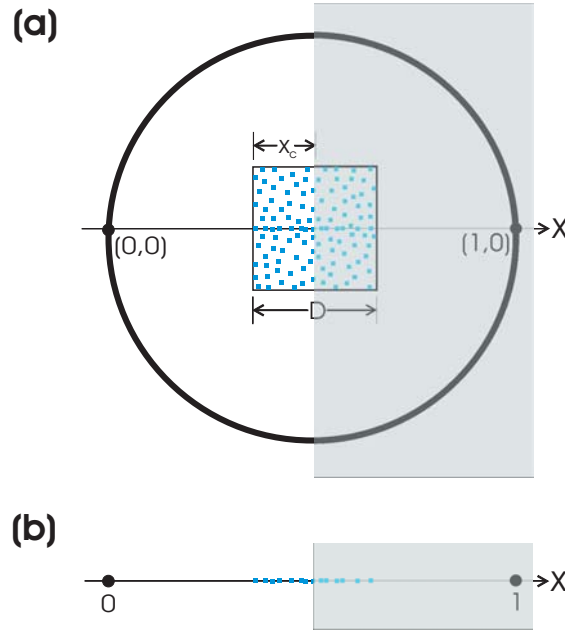


**Fig. 2. (a) Sketch of a 2-D perfect detector with a square speckle pattern from a multimode fiber. The gray box represents the source of obscuration in the problem. (b) 1-D representation of (a).**

Next, we evaluate how much detector noise is observed as speckles move on and off the obscuration edge. Given  $N$  speckles and the location of the obscuration edge, we choose random speckle locations over the interval of  $[0...D]$  according to a uniform distribution. We then observe the pertinent statistics of the Monte Carlo simulation, such as the mean and standard deviation of the signal, which then give the relative noise of the signal for each simulation. Fortunately, in this simple problem, there are simple equations that can be

derived for the statistics of interest. To model the relative noise of the signal, we use the binomial probability distribution.

The binomial distribution assumes an experiment with  $N$  trials, in this case,  $N$  speckles. The binomial distribution has only two outcomes, success or failure, and each of the speckle locations are independent of one another. The first step in the simulation is to use the binomial distribution to calculate the relative noise of the experiment. The probability for success,  $p$ , is  $x_c/D$ , which we rename as  $f_{\text{perfect}}$  because it will later represent the fraction of the area where a photodetector performs ideally. The probability for failure,  $q$ , is  $1-p$ . The mean signal was then calculated according to binomial probability theory:

$$\mu = N_{\text{speckles}} p . \quad (2)$$

The standard deviation of the signal is also obtained using binomial probability theory:

$$\sigma = \sqrt{N_{\text{speckles}} p q} . \quad (3)$$

The relative noise of the experiment is then defined as:

$$noise_{\text{relative}} = \frac{\sigma}{\mu} = \sqrt{\frac{q}{N_{\text{speckles}} p}} . \quad (4)$$

This equation gives the relative noise for the case where the transmission of the gray box is zero, which represents the inverse of the signal-to-noise ratio. In previous work, Kanada derived the same equation for the signal-to-noise ratio, equation 6 in reference [7], which is

based on Hill's original formula [2]. Note that Equation (4) has been experimentally verified in reference [2].

Next, we consider the case where the speckles are no longer infinitely small. Note that finite-sized speckles tend to slightly reduce the overall multimode fiber noise as seen in Fig. 3. Fig. 3 was produced using a Monte Carlo simulation where speckle size was allowed to vary. The  $\sim 10\%$  reduction in noise with increasing speckle size seen in Fig. 3 is small enough that we choose to ignore the effect in the remainder of this paper. We note that practical speckles are often small, especially in large core diameter fibers, high NA fibers, or in the ultraviolet wavelength range. For example, consider a multimode fiber with a core diameter of  $400\text{ }\mu\text{m}$ , an NA of 0.2, and a transmitted wavelength of  $300\text{ nm}$ . Using Equation (A10) below, we calculate the speckle diameter to be  $15\text{ }\mu\text{m}$  at a distance of one centimeter from the fiber (speckle size  $0.15\%$  of the beam size).

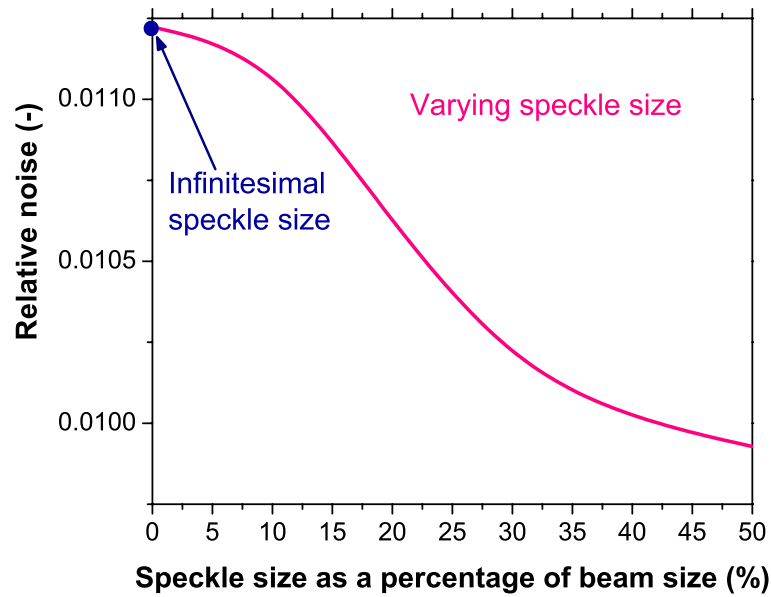


**Fig. 3. Comparison of the relative noise values for varying speckle size, by Monte Carlo simulation. The fiber diameter in this case is 200  $\mu\text{m}$ , the  $NA$  is 0.2, and the wavelength is 310 nm.**

To extend Kanada's work, we now assume the gray box is no longer opaque, but a variable density source of mechanical clipping. Practically, this represents a case where a neutral-density filter partially clips the beam. Although this exact situation is not common, the results will prove useful below. To simulate this condition, we must correct the probability for the transmission of the gray box, which will result in a new probability  $p'$ . The formula for  $p'$  is as follows:

$$p' = p + Tq, \quad (5)$$

where  $T$  is the transmission of the gray box. Physically, this equation simply gives each speckle landing in the partially transmitting region the appropriate credit. The new mean signal is calculated as:

$$\mu' = N_{\text{speckles}} p'. \quad (6)$$

In order to correct for the transmission in the standard deviation, one needs to multiply the standard deviation from Equation (3) by  $1-T$ :

$$\sigma' = (1 - T)\sigma. \quad (7)$$

Physically, this equation simply scales the original standard deviation to a smaller value in accordance with the fact that light transmitted through the obscuration acts to reduce the noise level associated with speckle motion. The relative noise of the signal is then given by:

$$noise_{relative}' = \frac{\sigma'}{\mu'} = \frac{1-T}{p+Tq} \sqrt{\frac{pq}{N_{speckles}}}, \quad (8)$$

which accounts for a variable transmission in the mechanical source of clipping.

Next, we wish to extend the above results to the case where multiple regions of reduced transmission can lie anywhere in the beam's cross-section. Fortunately, this extension is trivial; it turns out that neither the shape of the beam nor the shape of the masked area affect  $\mu'$  or  $\sigma'$ . This is because the binomial theorem is based only on the probability of the successes, not their locations. One can also reason, following Equation (2), that  $\mu'$  only depends upon the probability for success and the number of speckles; thus  $\mu'$  will not change simply by redistributing the speckles or masked areas in space. Using similar arguments relative to Equation (3), one can also reason that  $\sigma'$  will be independent of the shape of the reduced transmission region.

The above results represent a useful tool for predicting the mode noise produced by a multimode fiber [8]. The analysis developed considers the fraction of masked detector area and the transmission of that area. In practical applications, this algorithm can be used to analyze experiments that involve dirty or imperfect optics. In the following examples, we model mode noise using a wavelength of 1  $\mu\text{m}$ , and a multimode fiber with a numerical aperture of 0.2 and a core diameter of 200  $\mu\text{m}$ . By defining the fraction of unmasked area,  $f_{\text{perfect}}$ , and the transmission of the masked area,  $T$ , the simulation can represent the amount of imperfections on an optic and predict the noise associated with it. For example, imagine we have a window where 65% of the area is imperfect, and the transmission through the imperfect regions is 10%. This might be a common case for the window on a running engine

in our group's work [9]. In the algorithm we define  $f_{\text{perfect}}$  as 0.35 and  $T$  as 0.1, which results in a relative noise of 0.0424. This noise level is too high for most of our spectroscopic applications, so that we are generally forced to use single-mode fiber for launching sensor light into engines. Another practical application that can be modeled by this algorithm is the case of a non-uniform detector. In this case,  $f_{\text{perfect}}$  represents the section where the detector is perfectly uniform. The transmission, on the other hand, represents the responsivity of the detector in all regions where the detector is not perfect. By using the algorithm in this crude two-level method to model a non-uniform detector, one can estimate the noise associated with the detector. For example, consider a detector with a responsivity of one hundred percent over ten percent of the area and a responsivity of eighty percent over the remaining ninety percent of the area. In the algorithm we define  $f_{\text{perfect}}$  as 0.1 and  $T$  as 0.8, which results in a relative noise of 0.00216 using the same input fiber conditions as the dirty window example. Another situation to consider is one where a lens is dusty. When modeling a dusty lens we will assume most of the area is unmasked by the dust, and the fraction of the lens area that is covered in dust will not transmit light ( $T=0$ ). In this example, we define  $f_{\text{perfect}}$  as 0.98 and  $T$  as zero, which results in a relative noise of 0.00505 using the same input conditions as the previous cases. Finally, consider the case where a beam of light overfills the perfect detector being used. In this situation the unmasked area is considered the detector area, and the masked area is the area where the light has fallen off the detector, which will have a transmission of zero. We will consider the case where the beam of light area is four-thirds the size of the detector area. In this case, we define  $f_{\text{perfect}}$  as 0.75 and  $T$  as zero, which results in a relative noise of 0.02041, again using a wavelength of 1  $\mu\text{m}$ , a numerical aperture of 0.2, and a fiber core diameter of 200  $\mu\text{m}$ .



The relative noise of selected experimental situations including the cases described above is plotted in Fig. 4 in terms of several parameters. Two of those parameters are the transmission of the masked area and the fraction of the area that is unmasked. The relative noise is plotted versus the number of speckles, and for convenience versus a fiber diameter on the top x-axis. By examining Fig. 4 we can compare the levels of relative noise for the cases of an imperfect optic, a dusty lens, a non-uniform detector, and a few other situations with varying transmission and unmasked area fraction.

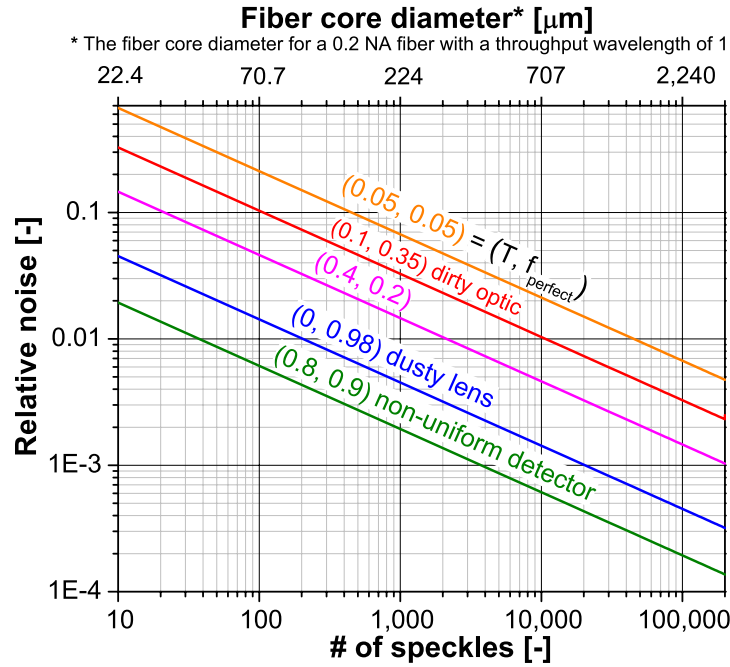


**Fig. 4. The relative noise versus the number of speckles for different cases of transmission and area fraction of the perfect detector.**

In this paper we have developed an algorithm to model fiber mode noise in terms of input launch conditions and fiber orientation. Another factor that affects the fiber mode noise is the wavelength of the input light. As the input wavelength is tuned using a tunable laser, the

speckle pattern changes at the output of the multimode fiber. By sending multiple wavelengths through a multimode fiber simultaneously, a speckle pattern develops for each wavelength. By averaging all the speckle patterns associated with each wavelength, the fiber mode noise is reduced. This situation occurs, for example, in the experiment of Fig. 1, where white light is detected after transmitting the finite spectral bandpass of the OSA. We hope to describe the detailed effects of spectral averaging in a future paper.

## **II.5 SUMMARY AND OUTLOOK**

An algorithm has been developed to predict the relative noise of a signal based on the multimode fiber characteristics. This algorithm will be useful for estimating the amount of mode noise created by introducing a multimode fiber into an optical system, which then can aid in estimating the signal to noise ratio in an experiment. The results in this paper apply to any analog signal noise involving a multimode fiber followed by any non-uniformity. Absorption spectroscopy is one experimental application of this paper, but there are many others in which this algorithm would be useful. This algorithm was developed based on several assumptions. The first assumption states that the V number of the fiber must be much greater than 2.405 (see Equation 1). This is assumed because the fiber has to transmit many modes in order to develop the infinitesimal speckles upon which our algorithm is based. The next assumption applied in this paper is that the multimode fiber is long enough where the modes reach the fully-filled condition in the fiber. Strictly, this condition requires several kilometers of fiber but is often approximated in fibers that are at least a few meters long. We also assume that the coherence time of the light source is much larger than the pulse broadening time of the fiber so that the propagating modes interfere within the fiber.

The next assumption states that there are only 2 regions: one where the transmission is perfect and one where the transmission is defined by the user. This means that there cannot be more than two transmissions,  $T=100$  and  $T$  defined by the user. The final assumption is that no spectral averaging is present. Spectral resolution in experiments using broadband light is an important consideration in many optical sensors, and therefore we plan to treat this case in a future paper. Even though this algorithm is based on many assumptions, it often represents a convenient engineering estimate to the amount of noise introduced by multimode fibers.

## II.6 ACKNOWLEDGEMENTS

The authors would like to thank Dr. Dmitry Kieseewetter for providing the speckle equations, Drew Caswell for help in deriving the speckle radius equation, and Ben Conrad for help in acquiring the MMF/SMF test data.

## II.7 REFERENCES

1. R. E. Epworth, "Phenomenon of modal noise in fiber systems," in *Optical Fiber Communication*, 6-8 March 1979, 1979, pp. 1-106.
2. K. O. Hill, Y. Tremblay and B. S. Kawasaki, "Modal noise in multimode fiber links: theory and experiment," *Opt. Lett.*, vol. 5, pp. 270-2, 06. 1980.
3. G.C. Papen and G.M. Murphy, "Modal noise in multimode fibers under restricted launch conditions," *J Lightwave Technol*, 17:5, 817-822 (1999).
4. Chia-Hung Chen, R. O. Reynolds, and A. Kost, "Origin of spectral modal noise in fiber-coupled spectrographs," *Appl Opt*, 45:3, 519-27 (2006).

6. G. Keiser, "Optical fibers: Structures and waveguide fundamentals," in *Optical Fiber Communications* , vol. 15, Anonymous 1983, pp. 34-39.
7. L. A. Kranendonk, J. W. Walewski, T. Kim and S. T. Sanders, "Wavelength-agile sensor applied for HCCI engine measurements," *Proc. Comb. Inst.*, vol. 30, pp. 1619-1627, 2005.
8. T. Kanada, "Evaluation of modal noise in multimode fiber-optic systems," *J. Lightwave Technol.*, vol. T-2, pp. 11-18, 02/. 1984.
9. S. T. Sanders, "Fiber mode noise calculator," Center for Hyperspectral Photonics, <http://chyp.erc.wisc.edu/index.php?page=tools>, September 2007.
10. L. A. Kranendonk and S. T. Sanders, "Optical design in beamsteering environments with emphasis on laser transmission measurements," *Appl. Opt.*, vol. 44, pp. 6762-6772, November. 2005.

## II.8 APPENDIX I

We start with the geometric equation for the radius of a circular beam of light emitted from the fiber:

$$r_{beam} = NA \times L , \quad (A1)$$

where  $L$  is the distance from the fiber face to the position of measurement. Next, the equation for the radius of each speckle will be derived. We begin the derivation in the near field by using the electric field equation for a field of waveguide modes:

$$E \propto J_l\left(\frac{ur}{r_o}\right), \quad (\text{A2})$$

where  $J_l$  is the energy of the electric field, and  $u$  is the eigenvalue of a mode. Next, we will approximate the energy of the electric field as:

$$J_l(z) \approx \sqrt{\frac{2}{\pi z}} \sin\left(z - \frac{l\pi}{2} - \frac{\pi}{4}\right), \quad (\text{A3})$$

which will then be substituted into Equation (A2) to give:

$$E \propto \sin\left(\frac{ur}{r_o}\right). \quad (\text{A4})$$

The range for the parameter  $u$  goes from 0 to the maximum value of  $V$ , which is defined as the characteristic  $V$  number of a fiber as given by Equation 1. When substituting the  $V$  number equation into the approximation for the electric field, we obtain:

$$E \propto \sin\left(\frac{Vr}{r_o}\right) \propto \sin\left(\frac{2\pi r \times NA}{\lambda}\right). \quad (\text{A5})$$

The next step is to equate the argument with the null half-cycle,  $\pi$ , which is where  $\sin(x)=0$ .

The result is:

$$\frac{2\pi r \times NA}{\lambda} = \pi. \quad (\text{A6})$$

The speckle radius equation in the near field is found by solving for  $r$  in Equation (A6).

Therefore, the radius of a speckle is represented by:

$$r_{speckle} = \frac{\lambda}{2 \times NA}. \quad (A7)$$

The next step is to find the equation for the radius of a speckle in the far field. In the far field, the equation for the size of the emitted light from an aperture at a distance  $L$  is:

$$r_{aperture} = NA \times L. \quad (A8)$$

By solving for the  $NA$  in Equation (A7) and plugging it into Equation (A8) for the  $NA$  the resulting equality is:

$$r_{aperture} = \frac{\lambda L}{2r_{speckle}}. \quad (A9)$$

The next step is to define  $r_{aperture}$  as the radius of the multimode fiber core,  $r_o$ , since we are using light that is emitted from a fiber onto a surface at a distance  $L$ . Therefore, the equation for the radius of a speckle in the far field is:

$$r_{speckle} = \frac{\lambda L}{2r_o}. \quad (A10)$$

The equation for the number of speckles is then derived by dividing the area calculated from Equation (A1) by the area calculated from Equation (A10). The result is as follows:

$$N_{speckles} = \frac{1}{2} \frac{A_{beam}}{A_{speckle}} = \frac{1}{2} \frac{\pi r_{beam}^2}{\pi r_{speckle}^2} = 2 \left( \frac{r_o \times NA}{\lambda} \right)^2, \quad (A11)$$

which calculates the number of speckles emitted from a fiber at a distance  $L$ . The factor of one-half is included in the formula because the ratio of areas provides the total number of

light and dark speckles, and we are interested only in the number of light speckles.

## APPENDIX III. SUPERCONTINUUM GENERATION

### EXPERIMENT: *Generation of ultraviolet broadband light in a single mode fiber*

Renata Bartula, Joachim Walewski, and Scott Sanders

#### III.1 ABSTRACT

Ultraviolet broadband light spanning 337 – 405 nm was produced in a single-mode optical fiber primarily by stimulated Raman scattering. Pulses of 4 ns duration at 337 nm were coupled into a 50-m-long ultraviolet-grade fiber featuring single-mode operation in the 320-450 nm range. Significant spectral broadening was achieved with pulses of only  $\sim 10$  W peak power. Our experiments demonstrate the potential for a source with  $\sim 10^4$  times the spectral radiance of a quartz tungsten halogen lamp, which is currently used for many applications in this wavelength range.

#### III.2 INTRODUCTION

Ultraviolet (UV) broadband light is of great interest in applications such as spectroscopy, data storage, and biomedical analysis (see [1] and references therein), as well as optical sensing [2, 3]. Of particular interest in our laboratory is the measurement of broadband absorption spectra in engines, as discussed by Richter et al. [4]. Most of these applications currently rely on lamps for broadband UV light. However, the low spectral radiance of lamps is often a limitation, especially when high spectral resolution ( $\lambda/\Delta\lambda > 10,000$ ) is



required. A user-friendly, broadband laser-like light source in the UV range is therefore of significant interest.

Spectral radiance (power per spectral bandwidth per area per solid angle) is an important figure of merit in spectroscopic applications, as we explain in the following. A  $\text{TEM}_{00}$  beam ( $M^2 = 1$ ) is often desired, for example, to provide diffraction-limited focusing. Diffraction-limited focusing, in turn, enables desirable features such as high spatial resolution (e.g., microscopy) and high spectral resolution (e.g., high-resolution grating spectrometers require narrow input slits). To a close approximation, specifying  $\text{TEM}_{00}$  at a wavelength defines the product of the beam's cross sectional area and solid angle. This product is often termed 'extent', and is an invariant under imaging in the limits of geometrical optics (see, e.g., [5]). The extent is included in the denominator of the spectral radiance as the product of area and solid angle. Thus a beam with  $M^2 = 10$  will have roughly  $1/10^{\text{th}}$  the spectral radiance of an otherwise identical beam with  $M^2 = 1$ , so the spectral radiance appropriately credits the latter source. Finally, as is well known, sources with a high power per spectral bandwidth are useful for spectroscopy. Thus the power per spectral bandwidth is also included in the spectral radiance, crediting, for example, high-power sources that can pump a spectrally-narrow feature. As an example, ultraviolet white light generation as presented in this paper can be compared to a commercially available ultraviolet LED in the same spectral range (e.g., Nichia i-LED). Because it is emitted with a low viewing angle from a single-mode fiber rather than a large viewing angle from a  $\sim 1\text{mm}$  area, the extent of the supercontinuum is  $\sim 10^7$  less than the LED, and thus the LED generally falls short of the supercontinuum in terms of spectral radiance.

Throughout this paper we compare the average spectral radiance of various sources. For the sake of comparison, we characterize our source according to its hypothetical radiance at a pulse repetition rate of 250 kHz, even though the highest repetition rate that the laser used can achieve is 24 kHz. We chose 250 kHz to match the repetition rate of a source reported elsewhere, [6] and because sources appropriate for future embodiments of the supercontinuum generation reported here are readily available in the 100-kHz repetition range (e.g., CrystaLaser QUV-266-30).

The current trend in broadband generation of light is to couple ultrafast pulse trains into dispersion-managed photonic crystal fibers to generate supercontinua with varied properties. However, reaching the UV by this approach is challenging due to a very high material dispersion in the UV (e.g. -1.834 ns/nm/km in fused silica at 350 nm). In ordinary optical materials, the dispersion is so high that it is difficult to compensate with custom fiber microstructures. To generate continua in the midst of such extreme dispersion, at least five approaches have been suggested. All but one are based on ultrafast lasers.

The first method is to use wavelengths where microstructured fibers and ultrafast lasers are readily available (e.g., near 750 nm), and attempt to create a continuum that extends to the UV. For example, several groups have used femtosecond pulses from a titanium:sapphire laser at a wavelength near 800 nm. These pulses were then coupled into photonic crystal fiber, which produced a broad supercontinuum ranging from 300 to 1600 nm [6, 7]. However, at 350 nm, we estimated the spectral radiance for the supercontinuum produced by Price et al. to be 69700 W/nm/m<sup>2</sup>/sr, only 14 times that of a typical quartz tungsten halogen (QTH) lamp. Our white light, at the hypothetical 250 kHz repetition rate, has the potential to produce a spectral radiance  $\sim 10^4$  times brighter than a QTH lamp at 350 nm. The modest

increase in spectral radiance over a QTH lamp may be insufficient to warrant the added complexity of the Price et al.'s approach in most applications requiring broadband UV light.

The second approach is third-harmonic generation of broadband, near-infrared radiation, generally without subsequent continuum generation in the UV. The advantage, for researchers desiring intense UV light, is the direct conversion to the UV (avoidance of generating visible continuum at the expense of UV intensity). For example, ultra-short lasers can produce pulses of 10 fs length and 100 nm ( $\sim 1500 \text{ cm}^{-1}$ ) bandwidth around 800 nm. If these pulses are coupled into a third-harmonic frequency generator, typically consisting of two non-linear crystals, the maximum achievable bandwidth at  $\sim 267 \text{ nm}$  is  $\sim 2700 \text{ cm}^{-1}$ . In general the bandwidth is limited by the acceptance bandwidth of the non-linear crystals. For A typical oscillator (Femtosource 'compact' grade) produces 5.3 nJ pulses with an average power of 400 mW at the fundamental. Assuming a UV conversion efficiency of 20%, this translates to  $\sim 1\text{-nJ}$  pulses with an average power of 80 mW at 267 nm. Our continuum offers a  $5000 \text{ cm}^{-1}$  spectral width, a pulse energy of 46 nJ and a (250 kHz) average power of  $\sim 10 \text{ mW}$ . The two times larger spectral coverage and the more than 40 times higher pulse energy are desirable in many applications. The larger pulse energy is possible because optical damage thresholds occur at higher energies for longer pulses [8]. Additionally, the overall system price is lower for the continuum approach. Finally, the third-harmonic generated in crystals commonly accompanies a deteriorated transversal beam profile while the broadband light generated in our approach is in the  $\text{TEM}_{00}$  mode.

Third-harmonic generation was also demonstrated in photonic-crystal fibers by Fedotov et al. [9] and investigated in detail by Ivanov et al. [10]. With this approach, one readily generates light of  $1500 \text{ cm}^{-1}$  bandwidth around 375 nm. However, the conversion efficiency in such

fibers is below one percent [10], which is about twenty times lower than for efficiencies achieved in bulk crystals, and the UV radiation is inherently multimode, which makes it less useful for optical applications. In total, our approach offers higher conversion efficiencies by directly pumping with UV light and a single-mode transversal profile.

The third method, perhaps the most complicated, is to choose a microstructured fiber with the bluest possible zero-dispersion wavelength (ZDW), then pump this fiber on both sides of the ZDW at wavelengths where the group velocities of the pump beams are approximately equal. Genty et al. describe the possibility of creating a broadband blue spectrum by using a broad ultrafast pulse near 900 nm together with another ultrafast pulse near 450 nm in a fiber with a ZDW near 650 nm [1]. They show that continuum generation in the visible to near-UV range is possible by carefully choosing the correct center pump wavelength and dispersion profile of the fiber [1]. Unfortunately, reaching shorter wavelengths becomes an increasing challenge to a method that is already complex.

The fourth approach suggested for UV continuum generation is to use an ultrafast pulse with high enough energy to sustain sufficient spectral broadening in a short ( $\sim 500 \mu\text{m}$ ) length, thus circumventing pulse walk-off. Theberge et al., for example, generated a supercontinuum in air extending to 230 nm [11]. Another group generated white-light continua between 400 and 700 nm by focusing picosecond pulses into glass [12]. Unfortunately, the pulse energies required in such continuum generation often require expensive, bulky laser systems. Furthermore, because the continuum is generated in bulk material, the quality of the transversal mode profile varies. In contrast, continua generated in single-mode fibers generally retain high mode quality.

The fifth approach for generating UV broadband light, our approach, is the simplest and therefore possibly the most likely to see widespread use. In this approach, sufficiently long optical pulses (or even CW lasers) are used to circumvent pulse walk-off. In this long-pulse regime, the likelihood of optical damage is reduced relative to ultrafast strategies. However, the nonlinearities useful in the ultrafast approaches (such as self-phase modulation) are dominated by stimulated Raman scattering, so the broadband light generated is primarily red-shifted. However, the approach is certainly viable for creating UV continua, as demonstrated in this paper. The long-pulse approach was used in one of the original efforts in fiber-based continuum generation. Lin and co-workers [13] created a continuum in the  $\sim 400\text{-}500$  nm range; the details of their experiment are summarized in Section 3. We improve on their approach and achieve single-mode white light further into the UV.

The remainder of this text is organized as follows. The method and the apparatus for the generation of long-pulse UV white light is outlined in the next Section, after which we present our results followed by a summary and outlook.

### **III.3 GENERATION OF BROADBAND LIGHT**

#### **III.3.1 Basic principles**

Supercontinuum generation is caused by nonlinear processes such as stimulated Raman scattering (SRS) and self-phase modulation (SPM) [13]. SPM broadens the spectrum of the input pulse, while SRS creates a series of stokes-shifted peaks on the red side of the pump wavelength. Self-phase modulation requires rapidly-changing, high-intensity light, as on the flank of an ultrafast pulse. For pump durations in the nanosecond regime, SRS and four-wave mixing are typically the main mechanisms of supercontinuum generation. It is assumed

that SRS creates a wide range of Stoke-shifted frequencies, which are smoothed by four-wave mixing [14]. Since one commonly implies high coherence with the term supercontinuum, we refer to broadband light generated by mainly SRS (low coherence) as white light generation. In this paper we focus on the generation of broadband light by red-shifting a UV pump laser by the aid of SRS.

### III.3.2 UV design guide

In general, to maximize spectral broadening, one chooses a high irradiance (but low enough to avoid optical damage) and a long interaction length (but short enough to limit pulse walk off and attenuation).

The first consideration when designing a UV supercontinuum is the laser source. When choosing a laser, there are four key parameters that have to be specified. The first parameter is the pump wavelength, which should be chosen to be the bluest wavelength of the desired supercontinuum. The beam quality, the second parameter, has to have an  $M^2$  value equal to one meaning that the laser beam mode should be  $TEM_{00}$ . In order to maximize the irradiance, a continuous wave laser can be chosen, but this can increase the cost of the system, so a pulsed laser may be more appropriate. If a pulsed laser is used, there are two more parameters to be specified: the repetition rate and the pulse duration. The repetition rate should be chosen as high as possible to maximize the irradiance, and the pump pulse duration can be determined by the design analysis described later in this section.

When generating UV broadband light, the next consideration should be the fiber. There are three key parameters that should be carefully chosen: the interaction length, the core diameter, and the material. The first parameter that will be analyzed is the fiber length. If

the fiber chosen is too long, two problems can occur: pulse walk off and attenuation. The extreme dispersion of the fiber causes the pulse to elongate in the fiber, which reduces the local irradiance and in turn reduces white-light generation. If the fiber is too long, the light can be attenuated and a substantial amount of white light that is developed in the fiber is lost. Another factor in deciding the length of the fiber is cost.

We begin the interaction length analysis by considering the role of fiber attenuation in limiting the maximum length of the fiber. The attenuation of the fiber is characteristic of the fiber material and is a function of the wavelength. The transmission through a fiber can be characterized by the following equation:

**Equation 1**

$$T = e^{-kL},$$

where  $T$  is the transmission,  $k$  is the material absorption coefficient in  $\text{m}^{-1}$ , and  $L$  is the fiber length in m. By setting  $kL = 1$  for ease of analysis, a transmission of 36.8 % can be achieved for a specified length  $L$ , which should provide sufficient power output through the fiber.

Now that a fiber length has been chosen, pulse walk-off must be considered to determine the pump pulse duration. An important parameter of pulse walk-off is the group delay difference,  $\Delta t$ , which can be calculated using the following equation:

**Equation 2**

$$\Delta t = L \left( \frac{1}{v_{g, \lambda \min}} - \frac{1}{v_{g, \lambda \max}} \right)$$

where  $L$  is the fiber length,  $v_{g,\lambda_{\min}}$  is the group velocity at the minimum white-light wavelength and  $v_{g,\lambda_{\max}}$  is the group velocity at the maximum white-light wavelength. The group delay difference is simply the difference in output arrival times one would observe if two short pulses (one at  $\lambda_{\min}$  and one at  $\lambda_{\max}$ ) were input to the fiber at the same time. This equation overestimates the temporal width of a supercontinuum generated in a fiber because it assumes that the white light is generated at the input facet of the fiber and simply transmitted through the fiber.

Next, we define the pulse walk-off severity as the ratio of  $\Delta t$  to the pump pulse duration. If this ratio is  $\ll 1$  (e.g., very short  $L$ ), then there is essentially no pulse walk-off. If this ratio is  $\gg 1$ , then pulse walk-off is likely to limit white light generation. We arbitrarily define pulse walk-off severity = 1 as the approximate limit to the maximum length of the fiber. Since the pulse walk-off severity is equal to one, then the pump pulse duration can be determined from the ratio described above.

The next important fiber parameter is the core diameter. The core diameter was chosen so that the fiber acted as a single mode fiber at the desired wavelength. Single-mode operation was chosen to avoid burning of fiber surfaces due to spatial spikes in irradiance, and thus to maximize the irradiance of the laser pulses.

The last parameter to be considered when selecting a fiber is the fiber material. Another practical consideration is the Raman cross section of the optical material used. Since SRS is a nonlinear process, the spectral broadening sought is greatly enhanced by even modest increases in this cross section. To achieve larger cross sections than available through fused silica, one could choose other fiber materials or dope the host with, e.g., rare-earth atoms.



However, single-mode fibers in other than fused silica are not broadly available, and heavily doping the host material may dramatically lower the damage threshold and UV transmission of the fiber. For those reasons we chose standard fused-silica fiber, which had already been demonstrated to sustain noticeable white-light generation when pumped around 380 nm [13]. Since the Raman cross section scales roughly with the inverse third power of the wavelength, pumping at 337 nm with a nitrogen laser, as demonstrated here, entails a  $\sim 40\%$  larger cross section, which is one of the reasons why we observed white-light generation at much lower power levels than Stolen et al. (see Section 3).

An example calculation for the fiber interaction length and the pump pulse duration will be demonstrated for our arrangement. We started the interaction length calculation by finding the material absorption coefficient for our fiber, which was  $0.023 \text{ m}^{-1}$ . Then, for ease of analysis, we set  $kL = 1$  and solved for a length,  $L$ , that would lead to a reasonable 36.8% transmission. By plugging the values into Equation 1 and solving for  $L$ , the length turned out to be 43.5 m. Next, the pump pulse duration was solved for using Equation 2. Using the length of fiber found above,  $1.94 \times 10^8 \text{ m/s}$  for  $v_{g,\lambda_{\min}}$ , and  $1.98 \times 10^8 \text{ m/s}$  for  $v_{g,\lambda_{\max}}$ , the pump pulse duration turned out to be 4.53 ns. The actual pump pulse duration that was used in the experiment was 4 ns, which was close to the calculated value, but restricted by commercial availability. Therefore, using the 4 ns pulse duration to calculate the length of fiber needed, results in a length of 38.4 m. The actual fiber length used to create the broadband light was 50 m long, and this leads to a transmission of 31.7%, slightly less than the ideal situation.

### III.3.3 Optical arrangement

A schematic of the optical arrangement is shown in Figure 1. The light source used is an air-cooled nitrogen laser (Spectra Physics 337-Si). The center wavelength of the laser is 337.1 nm with a spectral bandwidth of 0.1 nm and a 4-ns pulse at full width at half maximum (FWHM). The collimated light from the laser was sent through a lens (Thorlabs, LA4716,  $f = 750$  mm). The light was then focused through a 50- $\mu$ m pinhole that was mounted on a

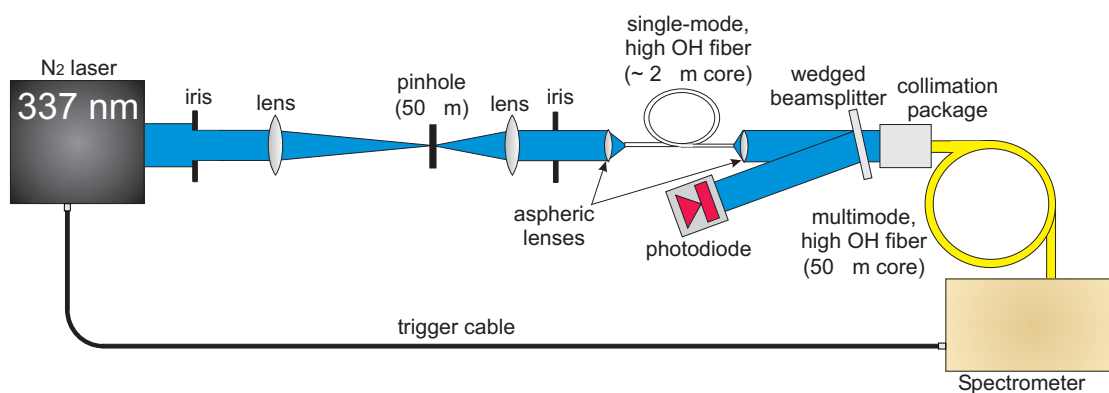


**Figure 1 – Schematic of the optical arrangement for the UV white-light generation. The light source wavelength is 337 nm and the light is monitored by a photodiode and analyzed by a spectrometer.**

sensitive XYZ flexure stage (Thorlabs MDT602). The pinhole was designed to transmit only the TEM<sub>00</sub> mode of the laser pulses. Once the light passed through the pinhole, it diverged to a lens (Thorlabs, LB4710,  $f = 300$  mm). This lens collimated the light, which was then directed onto an aspheric lens (Thorlabs, A397,  $f = 11$  mm). An iris was mounted between the 300-mm focal-length lens and the aspheric lens to eliminate diffraction rings created by the 50  $\mu$ m pinhole. The aspheric lens then focused the light onto a cleaved bare fiber (Stocker Yale, NUV-320-K1,  $\sim 2$   $\mu$ m core), which was secured by a fiber clamp (Thorlabs MDT711-250); both the aspheric lens and fiber assembly were mounted on a highly sensitive

XYZ flexure stage (Thorlabs MDT616). The light sent through the fiber was directed onto a second aspheric lens (Thorlabs, A390-A,  $f = 4.6$  mm), which collimated the light to a wedged beamsplitter. The light reflected off the beamsplitter was aimed onto a photodiode (Thorlabs DET210), and the transmitted light was coupled into a fiber (Ocean Optics, P50-2-UV-VIS, 50- $\mu\text{m}$  core) by aid of a collimation package. This multimode fiber was connected to a spectrometer (Spectra Physics 74050) with a frame transfer camera (Andor DV437-BU2-998). The photodiode served as a gauge for the pulse energies that were transmitted through the fiber, and the spectrometer recorded each transmitted spectrum in a single-shot. The spectrometer acquisition was triggered externally by each laser pulse.

### **III.4 RESULTS**

Single pulses of light at 337 nm were sent through the optical arrangement described above. As the total energy of each pulse increased, generally, the spectral range of the light was broadened, as shown in Figure 2. However, large pulse energies do not necessarily lead to greater spectral broadening. At present there is no explanation for this type of behavior. The spectral broadening is due to Raman pumping which is very efficient in the UV. At an initial energy of 1.5 nJ, recorded by the photodiode, a single pulse of light traveled through the bare fiber and created a single peak still at 337 nm. At higher energies such as 24, 34, and 31 nJ, the single pulse of light that traveled through the bare fiber created several peaks at a range of wavelengths initializing at 337 nm. At the highest energy, 46 nJ, the single pulse of light created many peaks ranging over 337 to 405 nm. The peaks are spaced by approximately 13.2 THz, consistent with the Raman gain profile in fused silica [15]. Note that the Raman pumping is so efficient that the pump power generally decreased as the input energy was

increased. Another factor contributing to this behavior is based on the attenuation losses of the fiber. The manufacturer specified attenuation values at 337 nm and 405 nm were 0.105 and 0.047 dB/m respectively. This corresponds to 30.0% transmission at 337nm and 58.5% transmission at 405 nm over the total 50 m length.

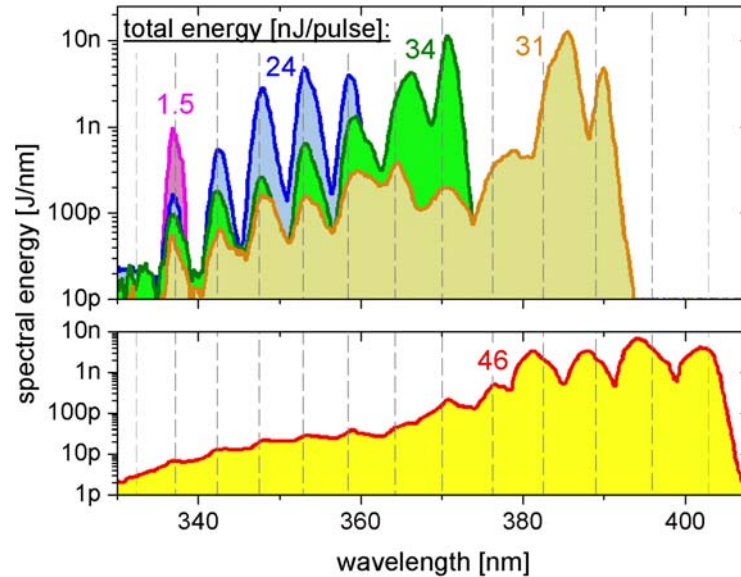


**Figure 2 – Graphs of the spectral energy versus the wavelength for several different energies. As the pulse energies increase broadband light with increasing bandwidth is generated. The gridlines shown are spaced 13.2 THz apart representing the Raman shift in fused silica. The spectral resolution of the measurement was 0.98 nm. The top graph shows actual data collected during the experiment. The bottom graph shows data that was collected during the experiment that saturated the detector. The data was corrected for the saturation of the detector. Notice however, that this correction is plagued with a substantial error, and the peaks above 370 nm are only qualitative.**

The single mode UV-VIS silica core fiber was susceptible to damage at the cleaved end due to intensity spikes in the transversal beam profile. Because of this, the light was coupled into the fiber during alignment at a much lower power than the power at which the broadband

light was generated. Once the coupling was fully optimized, an overall efficiency of about 4% was achieved. In our laboratories, we typically achieve  $\sim 70\%$  coupling efficiency into ordinary telecommunications fibers, and this 4% is considerably lower most likely due to challenges associated with the small core diameter of the UV single-mode fiber in addition to attenuation losses of 41.5 to 70% (depending on wavelength) throughout the length of the fiber. The major factor contributing to the low coupling efficiency is the imperfect surfaces of the aspheric lenses. The way aspheric lenses are produced creates an imperfect surface because of the machine tool used for the lens mold. In the infrared this does not create any coupling problems, but in the ultraviolet, the imperfect surfaces cause diffraction effects due to the significantly shorter wavelengths, which leads to a low coupling efficiency. However, the 4% figure is still reasonable for coupling a nitrogen laser, which produces beam profiles of notoriously low quality, into a single-mode fiber, and it is made possible by spatially filtering the laser with a  $50\text{ }\mu\text{m}$  pinhole before it reached the cleaved fiber. The light that traveled through the fiber in a single shot at 20 W per pulse generated a broadband light ranging from 337 nm to 405 nm.

In Table 1 we compare our results to those of Lin et al. [13]. Note that their continuum was produced with a pulse power of  $\sim 1\text{ kW}$  (where pulse power is defined as the ratio of the pulse energy to the FWHM pulse duration). They predicted that similar continua could be generated by coupling an order-of-magnitude lower pulse power into a longer fiber with a smaller core diameter [13]. This paper proves their prediction by attaining similar amounts of spectral broadening with a maximum pulse power of  $\sim 12\text{ W}$ . Even at  $\sim 6\text{ W}$  pulse power, significant spectral broadening was observed; at such low powers, one could consider generation of a continuous wave (CW) continuum, as described in section 4.

**Table 1 – Comparison of this work to a previous white-light generation experiment. The damage threshold was predicted with experimental data from technical papers on the topic of fiber damage [17], [19]. Wherever uncertainties or ranges are given, these are estimated.**

<b>Parameters</b>	<b>Units</b>	<b>“1976” (Lin et. al., 1976)</b>	<b>“2005” (this paper)</b>
Pump wavelength	[nm]	> 337.1	337.1
Maximum fiber-coupled pulse energy	[J]	10 $\mu$	(46.0 $\pm$ 3.0) n <sup>a</sup>
Pulse spectral bandwidth	[nm]	15	0.1 $\pm$ 0.01
Pulse duration	[ns]	10	4.0 $\pm$ 0.25
Maximum fiber-coupled pulse power	[W]	1000	11.5 $\pm$ 1.04 <sup>a</sup>
Physical fiber core diameter	[ $\mu$ m]	7	2.0 $\pm$ 0.1
Fiber numerical aperture		N/A	0.12 $\pm$ 0.01
Maximum fiber-coupled irradiance	[W/cm <sup>2</sup> ]	2.60 G	(366 $\pm$ 33) M <sup>a</sup>
Energy/area	[J/cm <sup>2</sup> ]	26	1.46 $\pm$ 0.09 <sup>a</sup>
Single-shot surface damage threshold	[J/cm <sup>2</sup> ]	~ 40	~ 30

“Chance of damage” <sup>b</sup>	[%]	65	5
Fiber length	[m]	19.5	50.0±0.5
Continuum spectral bandwidth	[nm]	145	68.0±2.0
Continuum spectral bandwidth	[%]	31.2	18.33±0.04
$\lambda_{\min}$	[nm]	392	337±0.1
$\lambda_{\max}$	[nm]	537	405±0.1
$v_{g,\lambda\min}$	[m/s]	$1.98 \times 10^8$	$1.94 \times 10^8$
$v_{g,\lambda\max}$	[m/s]	$2.02 \times 10^8$	$1.98 \times 10^8$
Transmission @ $\lambda_{\min}$	[%]	76.4	30.0
Transmission @ $\lambda_{\max}$	[%]	91.4	58.5
Group delay difference <sup>c</sup>	[ns]	2.0	5.21±0.05
Pulse walk off severity <sup>d</sup>	[-]	0.20	1.30±0.08

<sup>a</sup> Based on the output pulse energy of the pump laser.

<sup>b</sup> Defined as the ratio of the fiber-coupled pulse energy to the damage threshold.

<sup>c</sup> Defined as the difference in group delay for  $\lambda_{\max}$  and  $\lambda_{\min}$  over the entire fiber length assuming both wavelengths are generated at the input fiber facet.

<sup>d</sup> Defined as the group delay difference divided by the pulse duration.

Since the generation of broadband light reported here relies on nonlinear optical processes it consequently relies on high pump irradiances. It is not uncommon to exceed the surface

damage threshold of the fiber material upon super-continuum generation [16]. We assessed the potential of surface damage in our and Lin et al.'s experiment by comparing the surface damage threshold stated in the literature to the power densities in the experiments. The literature data was acquired for laser pulses at 800 nm, and the pertinent literature on laser damage does not offer an unequivocal dependence of the damage threshold on wavelength. However, studies of the bulk damage threshold clearly indicate a decrease of the threshold for a decrease in wavelength [17]. For the sake of simplicity we assumed a proportional dependence on the wavelength. According to Table 1 the “chance of damage”, which is based ratio between the energy density in the fiber and the surface damage threshold, is lower than 100%, i.e. the prevalent energy densities are not expected to result in a front-end damage of the fibers. However, as is well known these thresholds depend on particularities of the manufacturing process [17], contamination of input facet, etc. Another issue is the coupling of  $M^2 > 1$  light, since only part of the light will be coupled into the fiber, and the rest could lead to high irradiance on the input facet. Accordingly we recorded much lower thresholds than those reported in the literature (about a factor of ten to one hundred) when coupling the poor-quality laser profile into the single-mode fiber. Consequently we expect to increase the pulse energy of the super-continua generated in the fiber chosen by at least a factor of ten when coupling  $M^2 = 1$  light into the fiber.

### III.5 SUMMARY AND OUTLOOK

In this paper we demonstrated the ability to generate UV broadband light pulses with energies in the tens of nanojoules covering a spectrum from 337 to 405 nm when pumping at 337 nm. The maximum pulse rate of the nitrogen laser used was only 20 Hz, and thus the



setup presented here provided insufficient average power for most applications. A simple extension of this work would be to use a pump laser with a pulse rate in the kilohertz range to generate high average power. At a pulse rate of 250 kHz, the spectral radiance is some 35,000 times that of a Quartz Tungsten Halogen lamp. At the associated average power of only  $\sim 10$  mW and duty cycle of  $\sim 0.1\%$ , this higher repetition-rate pulse train is not expected to significantly compromise the damage threshold of the fiber.

Further extension of this work would be to use a pump laser that has not only higher repetition rate, but also at a wavelength deeper into the UV. However, this modification may meet challenges associated with solarization.

The per pulse energy of the generated broadband light can also be increased as may be required for certain experiments, or for the purpose of reaching higher average power levels. To pursue higher energies, a fiber with larger core diameter but still featuring single-mode operation is desirable. The appropriate fiber would have a UV-grade core, a larger core diameter, and a correspondingly lower NA. Fibers meeting all but the last requirement are readily available. For example, consider a fiber with a 50  $\mu\text{m}$  core diameter and a 0.12 NA (e.g., CeramOptec UV 50/125 A 12). Unfortunately this fiber is highly multimode (V-number = 54). An NA of 0.005 would be required for true single-mode operation of this fiber, and this NA is not currently feasible in such a fiber. Fortunately, the above fiber might be made to approximate an ordinary single-mode fiber by coiling it [18].

Finally, it is interesting to consider generation of CW white light in a  $\sim 2\text{-}\mu\text{m}$ -core single-mode fiber such as the one we used or perhaps in an endlessly single-mode photonic crystal fiber. As an example, we are considering to pump such a fiber with a high-power ion laser

(e.g., Coherent Sabre argon ion TSM-7). Such lasers offer  $\sim 7$  W total power distributed among several UV wavelengths (typically 351-364 nm), combined with  $\sim 25$  W total power distributed among several visible wavelengths (typically 458-515 nm). As demonstrated in this paper, such power levels are sufficient to produce significant spectral broadening. Owing to the CW nature of the light, pulse walk-off is not possible, permitting long fiber lengths limited only by attenuation. The multi-wavelength output of ion lasers is particularly attractive for creating ultra-broadband continua. For example, a continuum spanning the UV-visible range should be possible, and the 13.2 THz peak structures generated from each pump wavelength will act to flatten the continuum. A CW continuum with such high power over this entire range would certainly be useful; a 5W continuum would be 500 times brighter than a source operating at the hypothetical 250 kHz repetition rate, so all figures given relative to irradiance in this paper can be upgraded by a factor of 500. However, such high average power levels are likely to cause fiber solarization and damage, particularly in the UV. On a practical note, ion lasers are also inefficient and therefore expensive to operate and maintain.

### **III.6 ACKNOWLEDGEMENTS**

The authors thank Dr. Jaal Ghandhi for lending the spectrometer used to gather data. This material is based upon work supported by the National Science Foundation under Grant No. 0307455.

### III.7 REFERENCES

- [1] Genty,G., Lehtonen,M., and Ludvigsen,H., 2005, "Route to Broadband Blue-Light Generation in Microstructured Fibers," *Opt.Lett.*, **30**(7), pp. 756-8.
- [2] Lee,Y. C., Hassan,Z., Abdullah,M. J., Hashim,M. R., and Ibrahim,K., 2005, "Dark Current Characteristics of Thermally Treated Contacts on GaN-Based Ultraviolet Photodetectors," *The Proceedings of the 2nd International Symposium on Nano- and Giga-Challenges in Microelectronics, Sep 12-17 2004*, Anonymous eds., **81**(2-4), pp.262-267.
- [3] Yu-Zung Chiou, 2005, "GaN Ultraviolet Photodetectors with Transparent Titanium Tungsten and Tungsten Electrodes," *J.Electrochem.Soc.*, **152**(8), pp. 639-42.
- [4] Richter,M., Franke,A., Aldén,M., Hultqvist,A., and Johansson,B., 1999, "Optical Diagnostics Applied to a Naturally Aspirated Homogeneous Charge Compression Ignition Engine," *SAE International Fall Fuels and Lubricants Meeting and Exhibition*(1999-01-3649).
- [5] Nicodemus,F. E., 1976, "Self-Study Manual on Optical Radiation Mesurements: Part I," , pp. 84.
- [6] Price,J. H. V., Monro,T. M., and Furusawa,K., et al, 2003, "UV Generation in a Pure-Silica Holey Fiber," *Applied Physics B (Lasers and Optics)*, **B77**(2-3), pp. 291-8.
- [7] Travers,J. C., Popov,S. V., and Taylor,J. R., 2005, "Extended Blue Supercontinuum Generation in Cascaded Holey Fibers," *Opt.Lett.*, **30**(23), pp. 3132-3134.

- [8] An-Chun Tien, Backus,S., Kapteyn,H., Murnane,M., and Mourou,G., 1999, "Short-Pulse Laser Damage in Transparent Materials as a Function of Pulse Duration," *Phys.Rev.Lett.*, **82**(19), pp. 3883-6.
- [9] Fedotov,A. B., Yakovlev,V. V., and Zheltikov,A. M., 2002, "Generation of a Cross-Phase-Modulated Third Harmonic with Unamplified Femtosecond Cr:Forsterite Laser Pulses in a Holey Fiber," *Laser Physics*, **12**(2), pp. 268-272-4.
- [10] Ivanov,A. A., Lorenc,D., and Bugar,I., et al, 2006, "Multimode Anharmonic Third-Order Harmonic Generation in a Photonic-Crystal Fiber," *PHYSICAL REVIEW*, **73**(1), pp. 1-6.
- [11] Theberge,F., Liu,W., Luo,Q., and Chin,S. L., 2005, "Ultrabroadband Continuum Generated in Air (Down to 230 Nm) using Ultrashort and Intense Laser Pulses," *Appl.Phy. B*, **80**(2), pp. 221-225.
- [12] Alfano,R. R., and Shapiro,S. L., 1970, "Emission in the Region 4000 to 7000 A Via Four- Photon Coupling in Glass," , **24**(11), pp. 584-7.
- [13] Lin,C., and Stolen,R. H., 1976, "New Nanosecond Continuum for Excited-State Spectroscopy," *Appl.Phy.Lett.*, **28**(4), pp. 216-18.
- [14] Wadsworth,W. J., Joly,N., Knight,J. C., Birks,T. A., Biancalana,F., and Russel,P. St J., 2004, "Supercontinuum and Four-Wave Mixing with Q-Switched Pulses in Endlessly Single-Mode Photonic Crystal Fibres," *Optics Express*, **12**(2).

- [15] Islam, Mohammed N., 2002, "Raman Amplifiers for Telecommunications," IEEE Journal on Selected Topics in Quantum Electronics, **8**(3), pp. 548-559.
- [16] Walewski, J., Filipa, J., Hagen, C., and Sanders, S., 2005, "Standard Single-Mode Fibers as Convenient Means for the Generation of Ultrafast High-Pulse-Energy Super-Continua," Applied Physics B (Submitted.).
- [17] Kuzuu, N., Yoshida, K., and Ochi, K., et al, 2004, "Laser-Induced Bulk Damage of various Types of Silica Glasses at 532 and 355 Nm," Japanese Journal of Applied Physics, Part 1 (Regular Papers, Short Notes & Review Papers), **43**(5A), pp. 2547-8.
- [18] Koplou, Jeffrey P., Kliner, David A. V., and Goldberg, Lew, 2000, "Single-Mode Operation of a Coiled Multimode Fiber Amplifier," Opt.Lett., **25**(7), pp. 442-444.
- [19] Tien, An-Chun, Backus, Sterling, Kapteyn, Henry, Murnane, Margaret, and Mourou, Gerard, 1999, "Short-Pulse Laser Damage in Transparent Materials as a Function of Pulse Duration," Physical Review Letters, **82**(19), pp. 3883-3884 - 3886.

## APPENDIX IV. SPATIAL HETERODYNE SPECTROSCOPY

### EXPERIMENT: *OH absorption spectroscopy in a flame using Spatial Heterodyne Spectroscopy*

Renata Bartula, Jaal Ghandhi, Scott Sanders, Edwin Mierkiewicz, Fred Roesler, and  
John Harlander

#### IV.1 ABSTRACT

We demonstrate measurements of OH absorption spectra in the post-flame zone of a McKenna burner using spatial heterodyne spectroscopy (SHS). SHS permits high-resolution, high-throughput measurements: in this case the spectra span  $\sim 308 - 310$  nm with a resolution of 0.03 nm even though an extended source (extent of  $\sim 2 \times 10^{-7} \text{ m}^2 \text{ rad}^2$ ) was used. The high spectral resolution is important for interpreting spectra when multiple absorbers are present, for inferring accurate gas temperatures from measured spectra, and for monitoring weak absorbers. The present measurement paves the way for absorption spectroscopy by SHS in practical combustion devices such as reciprocating and gas-turbine engines.

#### IV.2 INTRODUCTION

Spatial Heterodyne Spectroscopy is an interferometric technique that was developed by Harlander and Roesler based on the Michelson Interferometer [1]. The mirrors of the two arms in the Michelson Interferometer are replaced by two gratings in the SHS instrument. As the light enters the instrument, it passes through a beamsplitter, which directs matched, planar wavefronts to each arm of the instrument where the gratings are located. The light

diffracted from the gratings is returned to a beamsplitter where the two wavefronts meet, now with a wavelength-dependent cross angle between them. The interfering wavefronts produce a Fizeau fringe pattern having wavelength-dependent spatial frequencies. The fringe pattern is then recorded by an imaging detector and is Fourier transformed to recover the desired absorption spectrum; details are provided in the literature [2-4].

### **IV.3 MOTIVATION**

A Spatial Heterodyne Spectroscopy (SHS) instrument was used to measure OH absorption near 308 nm in an ethylene-air flame produced by a McKenna burner. This is the first known application of SHS in combustion. Although dispersive solutions (e.g., the grating spectrometer, heretofore abbreviated as GS) are commonly used to measure ultraviolet spectra, they suffer from an inability to acquire high-resolution spectra with high throughput. Specifically, when using a GS, one must trade spectral resolution for optical extent; one can increase spectral resolution by reducing the input slit width and/or lengthening the focal length, but these measures also reduce the collection extent of the instrument. SHS was chosen over such conventional spectroscopy methods because of its intrinsic benefits. These benefits include a relatively large throughput, high spectral resolution, and compact size, benefits common to all interferometric spectrometers [5]. The primary advantage of SHS over conventional interference spectrometers is that SHS has no moving parts. Conventional interference spectrometers, such as a Michelson interferometer, are difficult to construct in the ultraviolet wavelength range due to present physical limitations of moving parts. The design tolerances for the moving parts scale with the wavelength requiring very precise and accurate movements in the ultraviolet range. Another advantage of SHS and other

interferometric techniques is the relaxed tolerances on element flatness, which arise due to the use of a multi-pixel camera as opposed to a single detector element [6]. By using a single detector element, imperfect optical flatness more severely increases the overall noise of the signal. The SHS instrument can also be field widened, generally by adding prisms between the beamsplitter and each grating, which can further improve the optical extent by approximately 2 orders of magnitude over the traditional SHS instrument [7]. In this paper, we explain how OH absorption was measured in a test flame using SHS and forecast future work on SHS applied to combustion problems.

Past OH absorption measurements in a firing Homogeneous Charge Compression Ignition (HCCI) engine at the Engine Research Center were made using a deuterium lamp (Hamamatsu model L7893), grating spectrometer (Oriel MS260i 1/4m), and kinetics-mode camera (Andor model DV437-BU2 back-illuminated CCD) [8]. Figure 1 presents a 200-cycle average spectrum at 6.2 crank angle degrees (CAD) after top dead center (aTDC). The

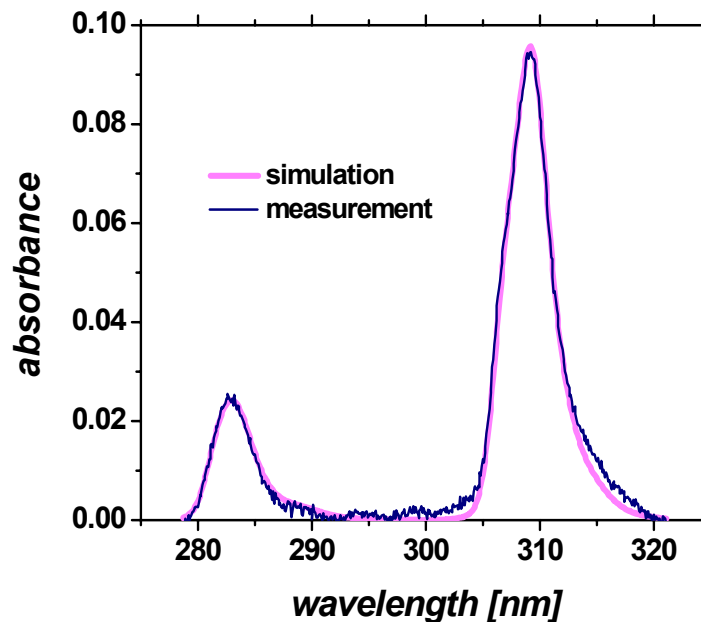




**Figure 1 – OH transmission data measured using a Deuterium lamp and grating spectrometer recorded in an engine running in HCCI mode on 10 mg n-Heptane per cycle with a 9.5 cm optical path length. This spectrum corresponds to a piston position of 6.2 CAD aTDC, and represents a 200-cycle average. Within the same measurement, similar spectra were recorded at other crank angles to allow us to monitor the evolution of OH in the engine.**

measurements were used to infer the mole fraction of OH versus piston location in a firing HCCI engine, but because the spectral resolution was too low to infer accurate temperatures, a H<sub>2</sub>O absorption sensor [9] was used for thermometry. The resolution of the previous measurement was 250 cm<sup>-1</sup>, corresponding to a resolving power  $R_0$  of 130. At this low resolution, several problems can occur when measuring and analyzing the OH spectra. These problems include: interference from other species, inability to infer accurate temperatures from the shape of the OH spectra, and an OH detectivity limited to ~ 1 ppm. Formaldehyde (CH<sub>2</sub>O) and other unidentified molecules, for instance, were seen to interfere with the OH spectra at certain engine operating conditions and crank angles, leading to a difficulty in identifying the true concentration of OH. Whereas the OH detectivity was near 1 ppm in these experiments, we predict we would be able to measure down to 100 ppb or better with higher-resolution spectra, even at a fixed signal-to-noise ratio. In fact, all of the above problems can be circumvented by acquiring higher resolution OH spectra, and SHS is a route to such spectra. The resolution of the SHS instrument described in this paper is 3 cm<sup>-1</sup>, which is 83 times better than the resolution of the GS results shown in Figure 1. In addition, the throughput increased by a factor of 10. The increased throughput can potentially relieve the need for cycle-by-cycle averaging.

In Appendix A, Fabry-Perot interferometers are compared with grating spectrometers in terms of optical extent and spectral resolution. The performance of the SHS instrument is assumed to be the same as the Fabry-Perot instrument since both instruments are ultimately subject to identical interferometric limits. Using Equation (a9),  $C = \frac{extent_{FP}}{extent_{grat\_spec}} = \frac{\pi}{\beta \tan \theta}$ ,

we can compare the extent of an SHS instrument with the extent of the imaging spectrometer used in the previous OH measurement at the Engine Research Center.  $\beta$  in Equation (a9) is defined as  $\tan(h/f)$ , which can be approximated as  $h/f$  for small angles, where  $h$  is the height of the pixel row or pixel rows used on the camera and  $f$  is the focal length of the GS.  $\theta$  in Equation (a9) is the blaze angle of the grating. The following experimental parameters, consistent with the measurements shown in Figure 1, were used in Equation (a9):  $\theta = 7^\circ$ ,  $f = 257$  mm,  $h = 0.325$  mm (a bin of 25 pixel rows at 13  $\mu$ m pitch). With these inputs, we find that an SHS instrument with the same resolving power and same grating size will feature an extent  $\sim 20,000$  times larger than the GS. This factor translates directly into performance gains. For example, a light source 20,000 times weaker could be used with the SHS instrument to achieve results similar to those shown in Figure 1. As a more likely example, the best available source would be used in conjunction with less averaging.

As another comparison, we consider a Princeton Instruments SP-2150i spectrometer and a Xenics XEVA-LIN CCD camera. The tall pixels and short spectrometer focal length increase the extent of the GS in this case, making it more competitive with SHS. The following grating parameters were used in Equation (a9) for this calculation example:  $\theta = 54^\circ$ ,  $f = 150$  mm,  $h = 500$   $\mu$ m. At fixed spectral resolution and grating size, the extent of the SHS instrument, in this case, is  $\sim 700$  times larger than the GS.

SHS interferometers are well suited for low light, high resolution spectroscopy, but they are not necessarily the best choice for all spectroscopic applications. For example, if the spectrum to be measured has both strong and weak content (as is common in Raman spectroscopy if the pump laser wavelength is not rejected by a spectral filter), the signal-to-noise performance of the GS may be favorable owing to the multiplex disadvantage [10]. In addition, preliminary computational comparisons of SHS and GS in absorption spectroscopy show an increased noise for the former at fixed camera SNR. Furthermore, SHS instruments are not widely available like grating spectrometers. Generally, grating spectrometers are the preferred solution if the extent and spectral resolution are sufficient for a given application. However, when the extent is insufficient, as is common in high-resolution spectroscopy at low light levels or high speeds, SHS solutions become attractive.

#### IV.4 SHS DATA

The SHS instrument is illustrated in Figure 2 in the boxed area. It consists of a spectral bandpass filter ( $\sim 3$  nm FWHM), a beamsplitter, and two matched gratings aligned at an angle of  $\sim 5.3$  degrees. The remainder of the experimental set-up is also pictured in Figure 2.

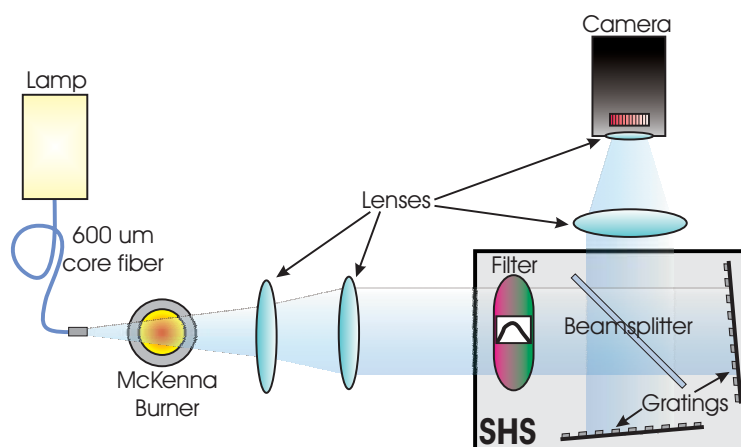


**Figure 2 – Schematic of the experimental arrangement including the SHS instrument (shown in the box labeled ‘SHS’). The goal of this experiment is to measure absorption spectra of OH contained in the combustion gases. The axis of the beam is ~ 22.5 mm above the height of the flame front and the beam diameter as it exits the combustion zone is ~ 11 mm.**

The light source is a Deuterium lamp (Hamamatsu, L7893) which is coupled into a multimode fiber (Ocean Optics, P600-1-SR, 600  $\mu\text{m}$  core diameter, 0.22 NA). A collimation package (Ocean Optics, 74-UV) is used at the distal end of the fiber to produce a 5 mm diameter beam that diverges at approximately one degree (half angle). The light expands over the McKenna burner which burns a stoichiometric mixture of ethylene and air, producing significant amounts of OH. The light is then sent through a telescope composed of an  $f = 125$  mm lens followed by a  $f = 200$  mm lens. The telescope delivers a ~ 40 mm diameter beam with ~ 0.45 degree half angle divergence to the SHS instrument. This beam then enters the SHS instrument through the input bandpass filter. The light is split by the beamsplitter and sent to each arm of the instrument. The light is then diffracted from the gratings in the Littrow configuration, so that the diffracted light in the first order nearly retraces the path back to the beamsplitter. The two wavefronts interfere once they are recombined at the beamsplitter. The output light is then sent through an output lens ( $FL = 300$  mm), which focuses the light onto a camera lens (UV-Nikkor, 105mm,  $f/4.5$ ). The image is then collimated onto the camera (Princeton Instruments, TE/CCD-1024-TKB) where the Fizeau fringes are apparent as seen in Figure 3. Although fringes are only visible in the stripe down the center of the image, other fine structure is present and is ultimately made visible by a Fourier transform.

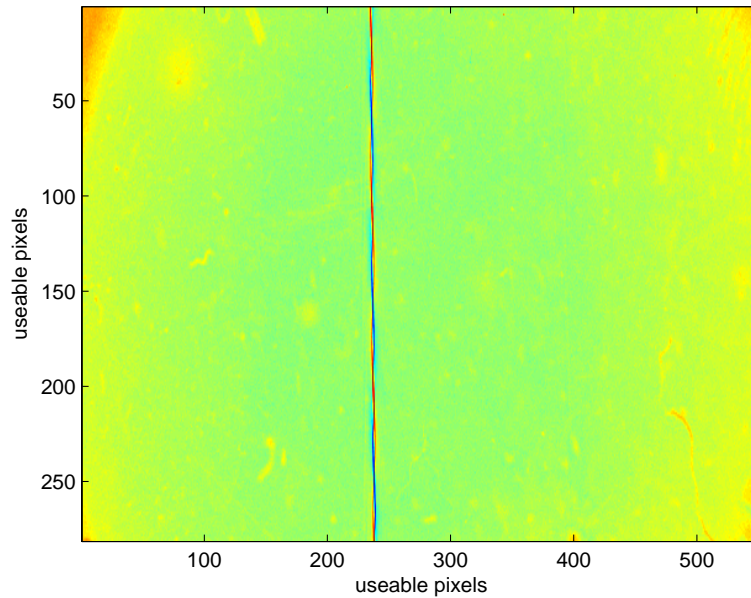


**Figure 3 – Image of the interferogram measured by the camera shown in Figure 2. Post-processing steps listed in the text have been applied to produce this image from the raw images.**

Our goal was to measure two experimental images:  $I_o(\lambda)$ , which is the spectrum of the lamp as seen by the camera, and subsequently  $I(\lambda)$ , which is the same spectrum but including absorption in the flame gases. The OH absorption spectrum is then readily obtained using absorbance,  $A = \ln \frac{I_o(\lambda)}{I(\lambda)}$ . The data processing for each experimental image is as follows:

1. A background correction is automatically applied by the camera to correct for the dark signal levels.
2. The SHS instrument background was corrected. Two pictures were taken with the light source on, each with one grating blocked. The average of these two pictures was subtracted from each experimental image. This step reduces noise due to imperfections in the gratings and beamsplitter; the set of SHS optics used here has many imperfections from years of handling, so this step was important.

3. A horizontal cut was used to select only 280 rows in the middle of each experimental image; the top and bottom contain little valuable information because they represent data falling near or past the edges of the gratings.
4. The mean of each experimental image was subtracted from the experimental image to eliminate the DC offset. A resulting  $I(\lambda)$  image from this step is shown in Figure 3.
5. The experimental image was windowed to reduce the edge effects of the interferogram; we chose a flat-top window here.
6. Zero padding the experimental image improves the final Fourier-domain results.
7. A 2-D Fast Fourier Transform was applied to the experimental image.
8. The rows of the result are finally averaged to create a 1-D OH spectrum for both  $I(\lambda)$  and  $I_0(\lambda)$ .
9. The resultant 1-D spectra,  $I(\lambda)$ , is divided by  $I_0(\lambda)$  to achieve the transmittance of OH in the flame.

Once the spectrum is post-processed, the arbitrary wavelength scale coming from the SHS data is adjusted to match that of a simulated spectrum computed using HITRAN [11]. The wavelength axis resulting from the FFT performed in the previous section is not automatically representative of a true wavelength scale. In our case, the OH spectrum spanned 0-550 arbitrary units rather than  $\text{cm}^{-1}$  or nm. In principle it is possible to compute a true wavelength axis directly from the FFT. However, in practice it is often more appropriate to warp the arbitrary axis to fit that of a simulated wavelength axis, which is the approach we followed here. The final OH absorbance results are shown in Figure 4. The measured OH spectrum was compared to OH simulations at atmospheric pressure and various temperatures.

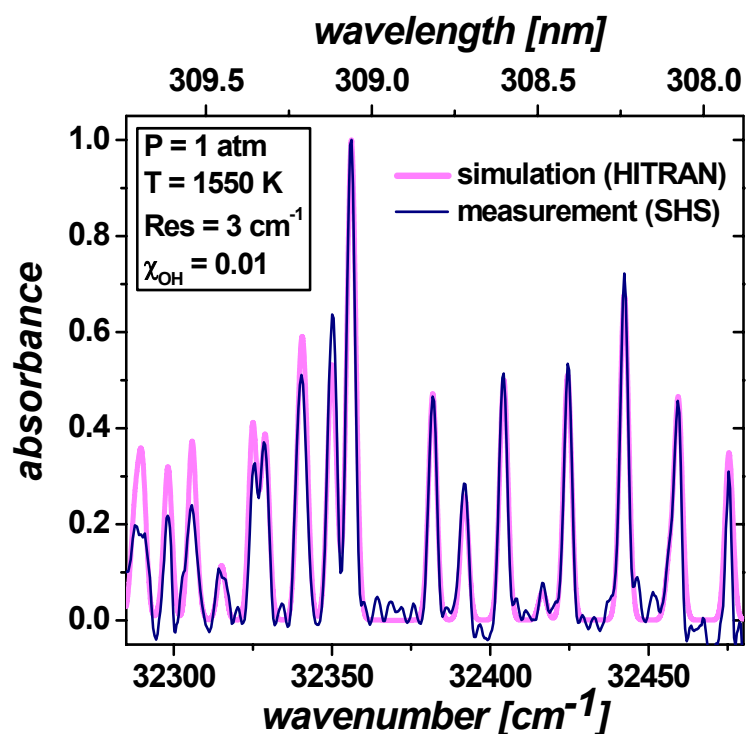


Figure 4 – Comparison of an OH spectrum simulated using HITRAN to an OH spectrum measured using SHS in the ethylene air flame. The simulation shown is chosen manually, but in the future selections can be done computationally as described elsewhere [12]. The simulation is smoothed to match the resolution of the SHS instrument measurement.

The simulated OH spectrum was convolved with a Gaussian profile to match the resolution of the SHS instrument, and the best fit temperature was 1550 K. The measured OH spectrum visually matches the simulated OH spectrum fairly well except for the left portion of the graph where the measured spectrum has systematically less absorbance than the simulated spectrum. This discrepancy has not yet been fully characterized; we suspect it is associated with low-frequency noise contaminating the interferogram, but it could be associated with other factors such as nonuniform OH properties in the flame. Based on our experience with H<sub>2</sub>O absorption thermometry in the 1355 nm range (see, e.g., [9], [12], [13]) we expect that

with further development we could achieve OH thermometry with a precision of better than 1% RMS. Furthermore, since the spectroscopy of diatomic OH is better known than the spectroscopy of H<sub>2</sub>O, the absolute accuracy of OH thermometry could be superior.

## IV.5 SUMMARY AND OUTLOOK

We have demonstrated the ability of an SHS instrument to resolve OH absorption spectra in a pre-mixed flame. This is the first known application of SHS in combustion. Combustion applications of spectrometers generally involve flowfield-induced beamsteering and use of fiber-optic cables. In this case of SHS, a multimode fiber was used to deliver the light to the flame zone, and beamsteering was introduced by the atmospheric-pressure gases in and near the flame. While we have not yet studied the negative effects of each in detail relative to SHS, the success of this experiment suggests that neither effect represents an insurmountable challenge.

The measurements of OH absorption spectra using SHS represent a spectral resolution 83 times better than OH measurements made in our center in an HCCI engine using a conventional GS. Furthermore, the SHS instrument has  $\sim 10\times$  higher throughput. In future work, we hope to apply a new SHS instrument, patterned after this one but designed specifically for HCCI engine studies, in our laboratories. The improved resolution and throughput are likely to enable combined measurements of gas temperature and OH mole fraction over a wide range of engine conditions.

In addition to absorption spectroscopy, as demonstrated here SHS is also likely to be useful for other spectroscopic modalities common in combustion diagnostics, including emission and fluorescence spectroscopy. Of particular interest may be Raman spectroscopy.



Typically, diagnostics based on spontaneous Raman scattering supply low light levels occupying a large extent to a spectrometer. Using SHS as the spectrometer for Raman scattering analysis, one is able to take advantage of the increased performance relative to throughput and spectral resolution that SHS has over grating spectrometers. In particular, SHS offers the ability to use ultraviolet wavelengths without compromising throughput or spectral resolution, potentially revolutionizing Raman spectroscopy.

## IV.6 ACKNOWLEDGEMENTS

The authors would like to thank Laura Kranendonk for the LabVIEW spectral warping code and Drew Caswell for the OH HITRAN simulation. Financial support is acknowledged by the DOE FreedomCAR and Vehicle Technologies University Project# DE-FC26-06NT42628.

## IV.7 REFERENCES

1. Harlander, J. M., Roesler, F. L., and Chakrabarti, S., "Spatial Heterodyne Spectroscopy: A Novel Interferometric Technique for the FUV," *Proc. SPIE* **1344**, 120-131 (1990).
2. Harlander, J. M., Reynolds, R., and Roesler, F. L., "Spatial Heterodyne Spectroscopy for the Exploration of Diffuse Interstellar Emission Lines at Far-Ultraviolet Wavelengths," *Astrophys.J.* **396**, 730-740 (1992).
3. Harlander, J. M., Roesler, F. L., Englert, C., Cardon, J., Stevens, M., Reynolds, R., and Jaehnig, K., "Spatial Heterodyne Spectroscopy: A Non-Scanned Method for High-Resolution Interference Spectroscopy," *Fourier Transform Spectroscopy Conference Proceedings, Quebec City, Canada*, 191-196 (2003).

4. Harlander, J. M., Roesler, F. L., Englert, C. R., Cardon, J. G., and Wimperis, J., "Spatial Heterodyne Spectroscopy for High Spectral Resolution Space-Based Remote Sensing," *Optics & Photonics News* **15**(1) 46-51 (2004).
5. Harlander, John M., Roesler, Fred L., Englert, Christoph R., Cardon, J., Conway, R., Brown, C., and Wimperis, J., "Robust Monolithic Ultraviolet Interferometer for the SHIMMER Instrument on STPSat-1," *Appl.Opt.* **42**(1), 2829-2834 (2003).
6. Englert, C. R., Harlander, J. M., Cardon, J. G., and Roesler, F. L., "Correction of Phase Distortion in Spatial Heterodyne Spectroscopy," *Appl.Opt.* **43**(3) 6680-6687 (2004).
7. Harlander, J., Roesler, F. L., and Reynolds, R. J., "The Field-Widened SHS: An Extremely High Etendue, Unscanned, Michelson-Based Spectrometer," in *Proceedings of the Astronomical Society of the Pacific* **71**, 336-337 (1995).
8. Younger, Sean, "OH Absorption Spectroscopy to Investigate Light-Load HCCI Combustion," University of Wisconsin-Madison, Masters (2005).
9. L. A. Kranendonk, R. Huber, J. G. Fujimoto and S. T. Sanders, "Wavelength-agile H<sub>2</sub>O absorption spectrometer for thermometry of general combustion gases," *Proc. Comb. Inst.* **31**, 783-790 (2007).
10. Fendel, S., Freis, R., and Schrader, B., "Reduction of the Multiplex Disadvantage in NIR FT Raman Spectroscopy by the use of Interference Filters," *J. of Molecular Structure* **410-411**, 531-534 (1997).
11. Rothman, L. S., Jacquemart, D., Barbe, A., Benner, C.D., Birk, M., Brown, L.R., Carleer, M.R., Chackerian Jr., C., Chance, K., Coudert, L.H., Dana, V., Devi, V.M., Flaud, J.M., Gamache, R.R., Goldman, A., Hartmann, J.M., Jucks, K.W., Maki, A.G., Mandin, J.Y., Massie, S.T., Orphal, J., Perrin, A., Rinsland, C.P., Smith, M.A.H., Tennyson, J.,

- Tolchenov, R.N., Toth, R.A., Vaner Auwera, J., Varanasi, P., and Wagner, G., "The HITRAN 2004 Molecular Spectroscopic Database," J. Quant. Spectrosc. Radiat. Transfer **96**, 139-204 (2005).
12. Kranendonk, L. A., Caswell, A. W., and Sanders, S. T., "Robust Method for Calculating Temperature, Pressure and Absorber Mole Fraction from Broadband Spectra," Appl. Opt. **46**(19) (2007).
13. Kranendonk, L. A., Sanders, S. T., An, X., Caswell, A. W., Herold, R. E., Huber, R., Fujimoto, J. G., Okura, Y., and Urata, Y., "High speed engine gas thermometry by Fourier-domain mode-locked laser absorption spectroscopy," Opt. Express, (2007 (Submitted)).
14. Jacquinet, P., "The Luminosity of Spectrometers with Prisms, Gratings, Or Fabry-Perot Etalons," J.Opt.Soc.Am. **44**(1), 761-765 (1954).

## IV.8 APPENDIX A

A quantitative comparison of a Fabry-Perot interferometer (FPI) and a grating spectrometer (GS) has been developed by Jacquinet [14]. Here we summarize Jacquinet's analysis and include additional equations for clarity. Fabry-Perot interferometers are compared with grating spectrometers in terms of optical extent and spectral resolution. The performance of the SHS instrument is assumed to be the same as the Fabry-Perot instrument since both instruments are ultimately subject to identical interferometric limits. Therefore, the comparison is for instruments of equal diffraction grating area,  $A_{grating}$ , and equal resolving power,  $R_o$ , defined by:

$$R_o = \frac{\lambda}{\Delta\lambda}, \quad (\text{a1})$$

Where  $\lambda$  is the central wavelength and  $\Delta\lambda$  is the spectral resolution. Given the area of the grating,  $A_{grating}$ , the extent will be solved for and compared for each instrument.

We begin the analysis for a GS by using Equation 1 in [14] as seen below:

$$extent_{grat\_spec} = \frac{S\beta\lambda D_2}{R_o}. \quad (\text{a2})$$

$S$  is defined as the normal area of the output beam,  $\beta$  is the angular height of the slits, and  $D_2$  is the angular dispersion at the output of the instrument. We then use Equation 3 in [14] as follows:

$$SD_2 = A_{grating} \left( \frac{2\sin\theta}{\lambda} \right), \quad (\text{a3})$$

to substitute into Equation (a2), where  $\theta$  is the blaze angle of the grating. The resultant equation is shown below:

$$extent_{grat\_spec} = \frac{A_{grating}\beta 2\sin\theta}{R_o}. \quad (\text{a4})$$

The extent for the grating equation needs to be in terms of the light incident upon the grating defined by the following equation:

$$A_{grating} = \frac{A_i}{\cos\theta}, \quad (\text{a5})$$

where  $A_i$  is the area of the light incident upon the grating. The resulting optical extent of the GS is:

$$extent_{grat\_spec} = \frac{A_i \beta 2 \sin \theta}{R_o \cos \theta}, \quad (a6)$$

and substituting  $\tan \theta$  in for  $(\sin \theta / \cos \theta)$  will result in the final grating extent equation:

$$extent_{grat\_spec} = \frac{A_i \beta 2 \tan \theta}{R_o}. \quad (a7)$$

Next, we use Equation 4 in [14] for the optical extent of the Fabry-Perot interferometer as follows:

$$extent_{FP} = \frac{2\pi}{R_o} A_i. \quad (a8)$$

The final step is to compare the extent of the Fabry-Perot interferometer to the GS. By combining Equations (a7) and (a8) we have the following comparison parameter:

$$C = \frac{extent_{FP}}{extent_{grat\_spec}} = \frac{\pi}{\beta \tan \theta}, \quad (a9)$$

where, once again,  $\beta$  is the angular height of the slit and  $\theta$  is the blaze angle of the grating.  $\beta$  is defined as  $\tan(h/f)$ , which can be approximated to  $h/f$  based on the paraxial approximation, where  $h$  is the effective linear height of the slit and  $f$  is the focal length of the spectrometer. Both  $\beta$  and  $\theta$  are strictly GS parameters, which remain in the comparison parameter,  $C$ .